university of groningen

faculty of science and engineering

Monolithic 4H-SiC Strip-loaded Waveguide and Optical Fiber Alignment Methods for Improved Future Optical EIT Control

Rick Beltman

Master's Thesis

To fulfill the requirements for the degree of
Master of Science in Physics: Advanced Materials
at University of Groningen under the supervision of

First Examinator: Prof. dr. ir. C.H. van der Wal
(Zernike Institute for Advanced Materials)

Second Examinator: Prof. dr. M.V. Mostovoy
(Zernike Institute for Advanced Materials)

Daily Supervisor: Joop Hendriks, MSc

July 11, 2023

Acknowledgments

This master thesis provides a summary of the work performed over the past year in the Quantum Devices (QD) team, in the cohort of the Physics of Nanodevices (FND) at the University of Groningen. For this I would like to thank a few people.
First of all, I would like to sincerely thank prof. dr. ir. Caspar van der Wal for allowing me to do my master research in his group. I have genuinely enjoyed the topic of quantum (nonlinear) optics and their possible applications in quantum telecommunication. Thank you for allowing me to continue doing research in your team and hopefully, in a couple of years, I will be writing the acknowledgments of a much larger manuscript.
Secondly, I would also like to thank prof. Maxim Mostovoy for examining my thesis, my presentation and for the many courses I have followed under your supervision.
I would like to express my deepest gratitude to my daily supervisor Joop Hendriks, for your guidance and teaching me innumerable amounts of tasks inside the lab. Although, the initial results were not exactly what we hoped for, we have greatly increased our knowledge about waveguides, which in the end has resulted in a working and promising rib waveguide platform. Without your extensive feedback this thesis would not have been made possible.
Furthermore, I would also like to thank our collaborators J. Ul-Hassan, N.T. Son, O. Trojak and A. Politi for their part in the creation of the waveguides.
Thanks should also go to my fellow master student colleagues, with whom I have shared an office, for their great discussions, help and just outright banter. I would like to especially thank my fellow QD colleague Adrian Sidhu. (I hope you are enjoying the nice weather of Barcelona, because you have deserved it!)
Lastly, I would like to thank the entire FND for the hospitality they have shown me and the great social events they have organised.

Abstract

The phenomenon of electromagnetically induced transparency (EIT) with divacancies in silicon carbide (SiC), is a suitable candidate to provide optical control for a quantum memory in quantum repeaters. The maturity of the SiC industry allows for the construction of complex electronic and photonic circuits, which can be used to improve EIT performance. Previous research focused on the application of a monolithic SiC slab waveguide, for increased optical confinement. This thesis is a continuation, where monolithic 4H-SiC strip-loaded waveguides are considered for a future platform for improved EIT measurements, due to the ability of confining light in two dimensions instead of one. To create a contrast in the index of refraction we used doping. However, the contrast that was realized was too low, resulting in a low confinement along the horizontal direction. The coupling of light into the waveguide was done using an optical fiber cable. Therefore, several optical fiber alignment methods were created, in order to increase the coupling efficiency. In addition, this allows for future attachment of the optical fiber to the waveguide, such that during EIT measurements no further alignment has to be performed. These alignment methods can be completed in minutes and allow for micrometer separation between the optical fiber and waveguide. For future research, monolithic 4H-SiC rib waveguides are proposed for their increased horizontal confinement. This work provides an improved understanding of waveguide mechanics and various complications that might occur.

Contents

1 Introduction

The advancements in telecommunication, which allows for almost instantaneous communication to anyone on the globe, has shaped the modern society. The next evolution is the inclusion of quantum properties like superposition and entanglement in computing and telecommunication [1]. One sought after application is that of quantum encryption, which allows for safe data transmission, due to the collapse of the quantum state when observed. However, this requires the transmission of entangled particles over long distances without the loss of coherence [2]. For this, the quantum repeater was proposed and investigated [3][4]. The phenomenon of electromagnetically induced transparency (EIT), has been used as a basis for the quantum memory inside these repeaters [5][6]. In addition, EIT has many applications in the field of sensing [7] and slowing down light [8]. The usage of silicon carbide (SiC) is an interesting platform for future quantum repeaters, due to the advanced semiconductor industry allowing for advanced electronic- and photonic-based circuits. In addition, divacancies in SiC have long spin coherence times [9], which are addressable in the telecom waveband [10]. This allows for easier and faster integration into the current telecommunication network, since no wavelength conversion has to take place.

The application of EIT in bulk crystals remains difficult, because of inhomogeneities due to strain. This causes an increase in the line-width of atomic transitions, also known as inhomogeneous broadening. To minimize this effect extremely pure crystals are required, which can only be achieved by growing SiC on an identical substrate. We work with the particular 4H-SiC polytype, which has a hexagonal crystal structure that repeats every four layers. The crystal structure of 4H-SiC, including a divacancy defect along the c-axis is shown in Figure 1. The defect is created by removing two neighbouring atoms, one carbon and one silicon, from the crystal structure. In order to increase the optical control of these defects, our group has experimented on monolithic 4H-SiC waveguides to confine light in one dimension [11]. The monolithic waveguide was doped in order to provide a contrast in the refractive index. Furthermore, doping allows for the creation of p-i-n diodes which have a wide range of applications, like optical sensing [12] and wavelength conversion [13]. This thesis is a direct continuation of the previous example, where a series of monolithic 4H-SiC strip-loaded waveguides on a single crystal have been manufactured. Strip-loaded waveguides allow for optical confinement into two dimension, which results in an even higher EIT performance by keeping the electromagnetic fields homogeneous over long distances. In our case, we want to keep the light confined over several millimeters to address as many defects as possible, before losses due to free-carrier absorption become too large (more information in sections **2.3.3** and **4.3**). Furthermore, micrometer precision is required to couple light into the waveg-

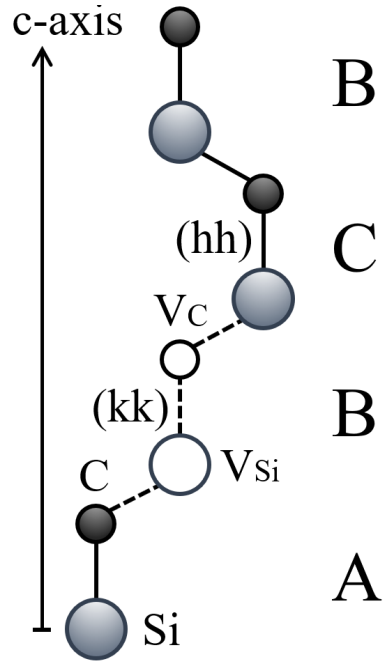

Figure 1: Schematic of crystalline structure of the polytype 4H-SiC with two atomic vacancies denoted by V_{Si} and V_C, resulting in a divacancy defect along the c-axis.

uide, which is difficult to obtain when the sample is located inside a cryostat for EIT measurements. Therefore, we want to permanently attach an optical fiber to the waveguide such that future alignments are not required. To attach an optical fiber to the waveguide, the optical fiber has to be aligned perpendicular to the waveguide facet. Therefore, we will develop several alignment methods that can be used to achieve this.

To summarize, this thesis focuses on the following problems:

Q1. Are monolithic SiC strip-loaded waveguides a suitable platform for future enhanced EIT control?

Q2. How to optimize the translational and angular alignment of an optical fiber for maximum coupling into a waveguide?

We will begin by looking at the basics behind the mechanics of EIT and how waveguides can be used to maintain complete transparency over long distances. Based on this, waveguiding mechanics in dielectric materials are explored. We look at how light propagate due to the principles of total internal reflection and in the form of optical modes, due to the self-consistency condition. Furthermore, we will discuss how we changed the index of refraction in our monolithic 4H-SiC crystal via the addition of dopants in the cladding and substrate layers. Depending on these refractive indices, the electromagnetic (EM) field distribution in a waveguide can be determined. For this we developed our own solver and compared it to the results of the effective index and wave-matching methods from SiIO, in order to better understand the physics behind (strip-loaded) waveguides.

In addition, the effects of different types of losses in waveguides are characterised. The most important of these losses will be due to free-carrier absorption, caused by doping the cladding and substrate layer. The magnitude of the free-carrier losses will be theoretically determined using a (new) developed equation and compared to different solvers from SiIO, Lumerical and previous experimental results. IFurthermore, we will also look at radiative losses when light travels through bends. This is important because our sample contains serpentine style bends and it is known that due to the low horizontal confinement in strip-loaded waveguides, these radiative losses become significant [14].

Finally, we will look at the optical coupling between an optical fiber and waveguide. For efficient coupling, the modes between the optical fiber and waveguide have to match, which is described by the butt-coupling method. The optical fiber has to be perpendicular to the waveguide surface and the separation between the optical fiber and waveguide should be minimal. To achieve this, two alignment protocols will be developed, one to align the angle and one to minimise the distance between the optical fiber and waveguide.

2 Theory

The following sections present a theoretical basis for EIT characteristics for divacancy defects in 4H-SiC. To maintain proper EIT, conditions regarding the optical excitation intensity, decay and dephasing rates of the system have to be considered. To satisfy these conditions over distances of a couple of millimeters to centimeters, optical waveguides are used. Therefore, the general dynamics of waveguiding in dielectric materials like SiC are explained, which will result in propagating optical modes. To create a contrast in the index of refraction, between layers in our monolithic 4H-SiC crystal, doping is used. Since the index of refraction is different for all layers, also known as an asymmetric waveguide, there are stricter requirements for the self-consistency condition which will be discussed. These general waveguide dynamics are used to describe the electromagnetic field distribution inside our strip-loaded waveguide and provide predictions on the confinement and shape of the propagating optical modes. Thirdly, we focus on the mode matching and coupling of light from an optical fiber to the waveguide, as described by the butt-coupling model. In addition, the effect of Fabry-Pérot interference on the total transmission, due to an etalon being formed between the optical fiber tip and waveguide, will be explored. Finally, different types of losses in waveguides are characterized to aid in future waveguide design.

2.1 Electromagnetically Induced Transparency for Divacancies in 4H-SiC

Similarly to NV centers in diamond, c-axis divacancy in 4H-SiC can be described as a local quantum system with spin $S = 1$. In this system, six energy levels are relevant for our description. These levels consist out of three ground states: $|g1\rangle$, $|g2\rangle$, $|g3\rangle$ and three excited states:$|e1\rangle$, $|e2\rangle$, $|e3\rangle$ [15]. The population in theses states can be controlled via optical pumping. In Figure 2 a simplified 3-level Λ scheme is shown, where the states $|g1\rangle$ and $|g2\rangle$ are optical excited by a probe and control beam to the state $|e2\rangle$. In reality, transitions into other states also occur, for instance the state $|g3\rangle$ is kept empty with optical pumping via a state that is not $|e2\rangle$, however for simplicity these are neglected [15]. The physics of the system in Figure 2 is described by the Hamiltonian $H = H_0 + H_{\text{int}}$, where H_0 is the bare defect Hamiltonian and H_{int} is the interaction with the driving fields. This interaction is given by the dipole approximation and is in general expressed using the Rabi frequency $\Omega = \vec{\mu} \cdot \vec{E}_0/\hbar$, where $\vec{\mu}$ is the electric dipole transistion and $\vec{E}_0$ the amplitude of the electric-field [16], resulting in the following Hamiltonian,

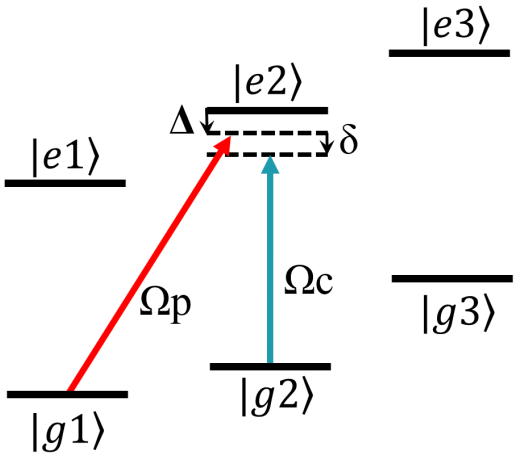

Figure 2: Divacancy energy levels, where two ground state levels g1 and g2 are coupled to one exited state e2 via a control and probe laser with Ω_c and Ω_p Rabi frequencies. Δ and δ denote single and two-laser detuning respectively.

$$H = -\frac{\hbar}{2}\begin{bmatrix} 0 & 0 & \Omega_p \\ 0 & -2\delta & \Omega_c \\ \Omega_p & \Omega_c & -2\Delta_p \end{bmatrix}. \tag{1}$$

In this Hamiltonian, Ω_p and Ω_c are the Rabi frequencies of the probe an control beam, Δ_p is the probe detuning from the $|g1\rangle$ to $|e2\rangle$ transition frequency and $\delta = (\Delta_p - \Delta_c)$ is the two-laser detuning [16]. For two-photon resonance, where $\delta = 0$, there exists an eigenstate that does not contain the excited state $|e2\rangle$ and is given by $|\Psi_0\rangle \propto \Omega_c|g1\rangle - \Omega_p|g2\rangle$. When the system is in this state, there is no possibility of spontaneous decay to another state, which is also known coherent population trapping (CPT). For a weak probe beam and strong control beam, i.e. $\Omega_p/\Omega_c \ll 1$, the absorption spectrum of the probe beam splits in two. The amount of splitting is related to the control beam Rabi frequency and causes increased transmission at the point of two laser resonance ($\delta = 0$). Therefore, this phenomenon has been named electronically induced transparency (EIT), as the transparency is controlled by the control beam. To determine the exact shape of the absorption spectra of the probe beam, the density matrix of the system has to be determined, which is generally done using the Lidbladian master equation. The specific element $\mathrm{Im}(\rho_{13})$ of the density matrix will then be proportional to the amount of absorption of the probe beam [16]. In Figure 3 the theoretical probe absorption is plotted for different control Rabi frequencies.

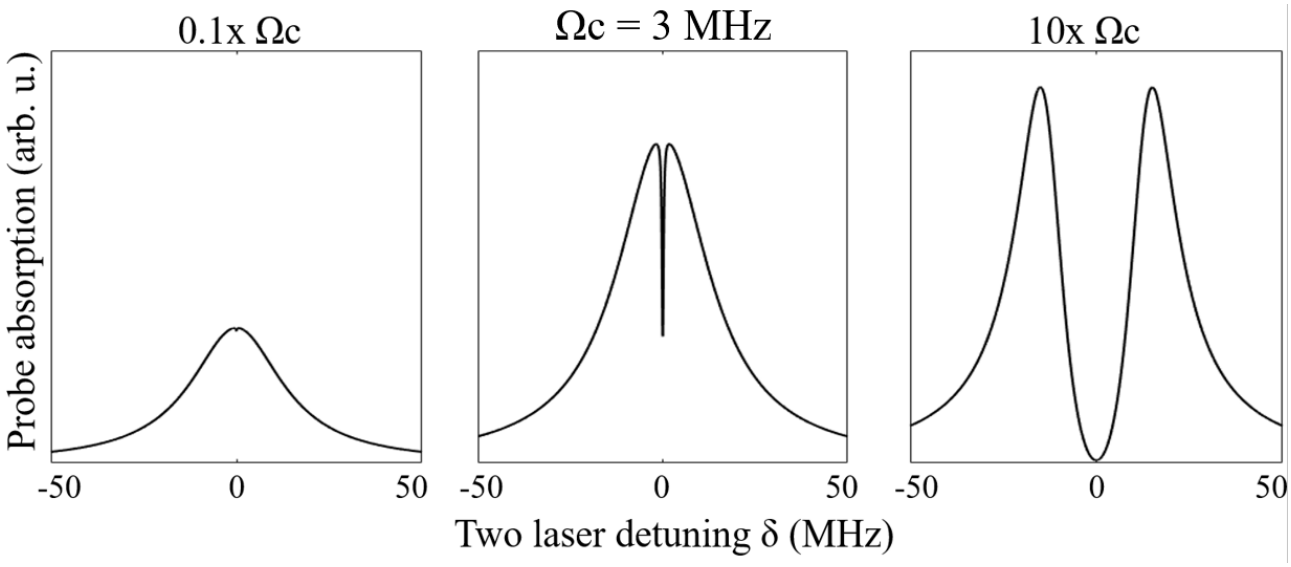

Figure 3: The effect of the control beam intensity on the EIT signature. In the center, the distinctive EIT dip can be seen at zero detuning. On the left the Rabi frequency of the control beam is lowered by a factor of ten, causing the absorption dip to vanish. On the right image the intensity is increased by a factor of ten and Autler–Townes splitting is observed. The strength of the probe beam is set to $\Omega_p = 10^4$ Hz and the decay and dephasing rates are given by: $\Gamma_e = 10^7$ Hz, $\Gamma_g = 10^4$ Hz, $\gamma_e = 0$ Hz and $\gamma_g = 10^5$ Hz, as determined from previous experiments and where g and e denote ground and excited state [15].

As can be seen, the important absorption dip feature of EIT is highly depended on the Rabi frequency of the control beam. Since the Rabi frequency depends on the electric-field via the

dipole interaction, the relation between Rabi frequency (Ω) and optical intensity (I) is given by, $\Omega \propto \sqrt{I}$. To maintain the narrow transmission window as shown in the center of Figure 3, the control beam has to satisfy the condition $|\Omega_c|^2 \gg (\Gamma_e + \gamma_e)\gamma_g$. But, to prevent wide Autler-Townes splitting, which is similar but not the same as EIT and is shown in the right image of Figure 3, the condition $|\Omega_c| < (\Gamma_e + \gamma_e)$ has to be satisfied. [16]. To satisfy these conditions, it is required for the control beam intensity to be homogeneous over distances on the order of several millimeters, such that a sufficient amount of divacancy defects are addressed. A problem with a standard lens and bulk- crystal based setup, is that the intensity of the light is only high near the focal point of the lens, but quickly diminishes as the beam diverges inside the bulk crystal. In a particular case it might be that at the focal point there is wide Autler-Townes splitting, followed a tiny region of narrow transmission and at the edges of the crystal a complete loss of the signal due to high absorption. Therefore, optical waveguides are being considered and used for enhanced control of EIT [17]. Waveguides allow for optical confinement inside a crystal over long distances, such that the intensity profile remains largely constant.

2.2 Dielectric Waveguide Mechanics

SiC is a dielectric for light at telecom wavelengths. Therefore, we look at the mechanics behind waveguiding in dielectric materials. In these waveguides, the phenomenon of total internal reflection is used to keep the light contained in a small region. When light is inside a region of higher refractive index than its surrounding, if the angle of incidence is smaller than some critical angle $\theta_c = \arcsin(n_s/n)$, where n_s and n are the respective refractive indices of the surrounding and guiding layer, then all of the light will be reflected. The light inside a waveguide is guided in the form of optical modes. For these modes to exist, the self-consistency condition has to be satisfied, which states that after two successive reflections the phase of the original wave should match that of the twice reflected wave (see Figure 4).

2.2.1 Optical Modes in Waveguides

Following the ray-optics description, it is assumed that light is a transverse electro-magnetic (TEM) plane wave. According to the self-consistency condition, these waves propagate at a specific angle called the mode angle θ_m and are called optical modes of the waveguide. In Figure 4 such a plane wave is depicted. For the phase fronts of the original and twice reflected beam to align, the phase shift induced by reflecting from the top surface, traveling from A to C and reflecting from the bottom surface should equal or be a 2π multiple of the phase of the original wave, while traveling from A to B [18]. This condition is described by the following equation,

$$2dk\sin(\theta) - \varphi_{r12} - \varphi_{r13} = 2\pi m, \qquad m = 0, 1, 2, ... \tag{2}$$

where the first term is the phase difference acquired from the difference in travel distance between the original wave (AB) and the reflected wave (AC). This difference in travel distance depends on the thickness of the guiding layer d, the wavenumber inside the guiding medium k and the angle of incidence θ. The other terms φ_{r12} and φ_{r13} are the phase shifts due to reflecting with the first and second layer respectively. The phase shift due to reflection can be determined from the Fresnel equations by taking the argument of the reflection coefficients. For transverse electric (TE) and transverse magnetic (TM) polarised waves this results in the following two equations [18],

$$\tan\left(\frac{\varphi_{\mathrm{TE}}}{2}\right) = \sqrt{\frac{\sin^2(\bar{\theta}_c)}{\sin^2(\theta)} - 1} \tag{3}$$

$$\tan\left(\frac{\varphi_{\mathrm{TM}}}{2}\right) = -\tan\left(\frac{\varphi_{\mathrm{TE}}}{2}\right)\frac{1}{\cos^2(\bar{\theta}_c)}, \tag{4}$$

where θ is the incident angle with respect to the surface and $\bar{\theta}_c = \pi/2 - \theta_c$ is the complementary critical angle. Inserting these phase shifts into equation (2) and solving for $\sin(\theta)$ numerically or graphically, the mode angle of the propagating wave can be determined. Depending on the mode angle the wave propagates with the following propagation constant β along the optical axis,

$$\beta_m = n_1 k_0 \cos(\theta_m) = n_{\mathrm{eff},\,m}\, k_0 \tag{5}$$

where n_1 is the index of refraction of the guiding layer, as shown in Figure 4, which can be combined with the cosine term to give an effective index of refraction n_{eff} and k_0 is the wavenumber in vacuum. The effective index of refraction decreases with the incident mode angle. This can be understood in the sense that the wave travels in a triangular way, bouncing around via reflecting with the interfaces. The effective index of refraction is a property of the guided mode and not the waveguiding material. This is an important distinction to make, because certain laws do not work with effective refractive indices like Snell's law, due to the light being an optical mode and not a plane wave. The notion of an effective index of refraction, for specific guided modes, will be used extensively for describing the horizontal confining properties of a strip-loaded waveguide.

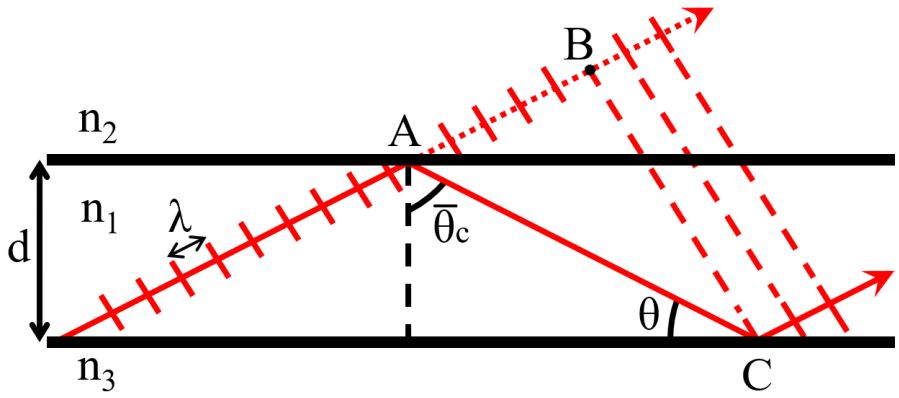

Figure 4: Schematic of the self-consistency condition in a dielectric waveguide with a guiding layer thickness d, where after two successive reflections at points A and C, the phase front of the original beam and twice reflected beam have to be equal or differ by a multiple of 2π. When the index of refraction n_1 is larger than both n_2 and n_3, then total internal reflection occurs when the incident angle θ is smaller than the complimentary critical angle, $\bar{\theta}_c = \pi/2 - \theta_c$ of both interfaces. The mathematical description of the self-consistency condition is given in equation (2)

2.2.2 Changing the Refractive Index via Carrier Concentration

For a waveguide to guide waves, it is required that the refractive index of the mediums around the waveguide core to be lower. But, in our case we use monolithic SiC, which has a singular index of refraction. To create a contrast in refractive index between different layers, carrier

concentration from doping can be used. At high enough doping concentration, the inclusion of negative (n) and positive (p) type dopants leads to a plasma of free electrons or holes. Upon excitation by an electromagnetic wave, with frequency ω, these free-carries are displaced and induce a polarisation in the material, which results in a relative permittivity ϵ_r as described by the Drude-Lorentz model [19].

$$\epsilon_\mathrm{r}(\omega) = \epsilon_\mathrm{opt} - \frac{Ne^2}{\epsilon_0 m^*}\frac{1}{\omega^2 + i\gamma\omega} \tag{6}$$

In this equation ϵ_opt is determined from the refractive index of the undoped material $\epsilon_\mathrm{opt} = n_0^2$. N is the doping concentration, m^* is the effective mass and γ is a damping rate related to free-carrier absorption. It is customary to split equation (6) into a real and imaginary part $\epsilon_\mathrm{r} = \epsilon_1 + i\epsilon_2$, resulting in the following two equations,

$$\epsilon_1 = \epsilon_\mathrm{opt}\left(1 - \frac{\omega_p^2\tau^2}{1+\omega^2\tau^2}\right) \tag{7}$$

$$\epsilon_2 = \frac{\epsilon_\mathrm{opt}\omega_p^2\tau}{\omega(1+\omega^2\tau^2)} \tag{8}$$

where ω_p is known as the plasma frequency $\omega_p^2 \equiv Ne^2/\epsilon_\mathrm{opt}\epsilon_0 m^*$ and $\tau = \gamma^{-1}$ is the damping time. In the regime of the infra red, where $\omega\tau \gg 1$ and $\omega \gg \omega_p$, the change in the refractive index Δn, following from the binomial approximation is given by,

$$\Delta n \equiv \sqrt{\epsilon_1} - n_0 \approx -\frac{n_0\,\omega_p^2}{2\,\omega^2}. \tag{9}$$

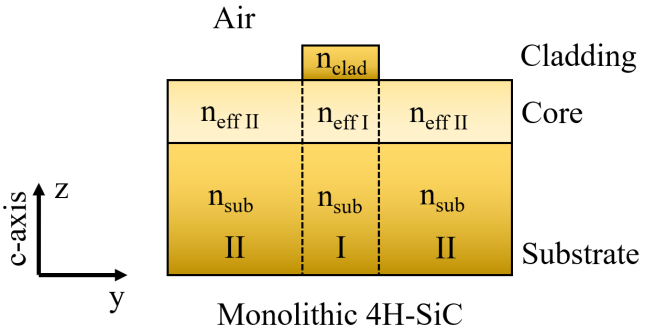

Figure 5: Schematic of the monolithic 4H-SiC strip-loaded waveguide. Each layer consisting out of a substrate, core and cladding/air layer, has a different refractive index due to carrier concentration induced via doping. The core layer is partitioned into two regions (I and II), as to denote the different optical properties generated by the loaded strip.

With this equation the change in refractive index can be calculated, depending on the doping concentration and type.Figure 5 shows the general structure of the strip-loaded waveguide. The inclusion of n-type doping in the substrate layer and p-type doping in the cladding layer changes the refractive index slightly to n_sub and n_clad respectively. The doping concentration in the core layer is around four orders of magnitude smaller than the cladding and substrate. Therefore, the index of refraction in the core (n_c) is almost identical to that of undoped 4H-SiC. Furthermore, the refractive index of the core layer is divided into two effective refractive indices, n_I and n_II given by equation (5), because each region is able to maintain a separate optical mode, as can be derived from the self-consistency condition according to equation (2). Since the substrate and cladding layers have different refractive indices, there are additional requirements for optical modes to exists. These asymmetric waveguide requirements are discussed in the following section.

2.2.3 Self-consistency Condition Requirements for Asymmetric Waveguide

In asymmetric waveguides, where the substrate and cladding layer do not have identical refractive indices, there exists the possibility that the self-consistency condition cannot be satisfied. This would result in a waveguide, that is not able to maintain any optical modes, or simply a waveguide that cannot guide waves. The fact that the self-consistency condition cannot be satisfied can simply be understood by the fact that at one of the interfaces, for instance the substrate-core interface, total internal reflection does not occur and a portion of the light is transmitted. When looking at equation (3), the phase φ_{TE} becomes imaginary when the incident angle exceeds the critical angle, i.e. there is no total internal reflection. Once the phase becomes imaginary, then no real solutions to the self-consistency condition given by equation (2) exists. In Figure 6, a graphical solution to equation (2) is given for both an asymmetric and symmetric waveguide. The graphical solution consists of finding the intersection of the first term in equation (2), with the combined phase terms for the zero order mode ($m = 0$). In the case there is no intersection, then there exists no solution to the self-consistency condition, resulting in a waveguide that cannot guide waves.

In total there are two contributions to the size of the gap in Figure 6(a). First of all, the greater the difference between the index of refraction between the cladding and substrate layer, the earlier one of the interfaces does not support total internal reflection. Secondly, the smaller the ratio in refractive index between the cladding/substrate and core ($n_{\mathrm{clad}}/n_{\mathrm{c}}$ or $n_{\mathrm{sub}}/n_{\mathrm{c}}$), the smaller the (complimentary) critical angle. This reduces the allowed mode angles, because $\theta_m < \bar{\theta}_c$ and thus stricter requirements for optical guiding. In short, we want to minimize the difference in refractive index between the cladding and substrate and maximize the ratio between the cladding/substrate and the core refractive index.

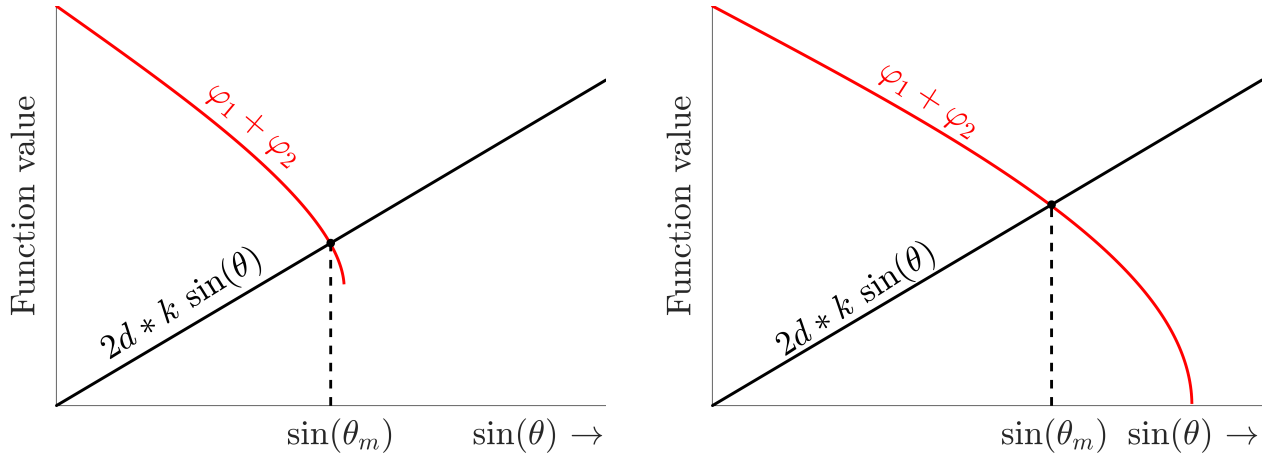

(a) Asymmetric cladding ($n_2 \neq n_3$) (b) Symmetric cladding ($n_2 = n_3$)

Figure 6: Graphical solution to the self-consistency condition for modes of a waveguide. (a) In an asymmetric waveguide, at a certain point one of the layers is not able to perform total internal reflection. This causes a gap in the combined phase terms, where there might not be a solution to the self-consistency condition. (b) In a symmetric waveguide there is always a solution to the self-consistency condition.

2.2.4 Electromagnetic Field Distribution in Strip-Loaded Waveguides

Finally, it is of interest to know the EM-field distribution inside waveguides. With said distributions we are able to predict properties such as the optical confinement and losses in the waveguide. To do this, we will use the full-mode description instead of the ray-optic method. This allows for the use of only one incident angle (instead of all incident angles smaller than the critical angle, for the ray-optic method). This angle is the mode angle θ_m as determined from the self-consistency condition described in equation 2. The full-mode description will not be able to take into account any pertubations in the incident angle due to surface roughness. But, because a majority of the light will be confined inside the core layer and the crystal is monolithic, the effect of surface roughness on the propagation of light is limited. There are many ways to solve the EM-field distribution by using mode solvers such as: finite element, finite difference, effective index, wave matching, etc. All mode solvers solve for Maxwell's equations, but each method uses different assumptions and/or complexities describing the optical modes [20][21]. Depending on the exact geometry certain solvers are more applicable than others. For instance, when a waveguide cannot be sliced into a set of slab waveguides, as was done in Figure 5, then the effective index method cannot be used. To improve our understanding of the physics and working principles of waveguides, an in-house solver is developed. By comparing the results to other more complex solvers, we can asses the accuracy/validity of our model/assumptions and understand the results of other simulations to a higher degree.

The solver that is used in this work, separates the waveguide according to the substrate, core, cladding and sliced regions I and II, as show in Figure 5. Depending on the optical properties of each region, the EM-field is either described by a sinusoidal function in a confining region (like the core layer) or described by exponential decay in non-confining regions (like the cladding and substrate layers). The exact solution is determined by ensuring continuity of the EM-field between each layer [14]. This relative simple method of describing the one-dimensional optical confinement of a slab waveguide is extended to describe the more complicated strip-loaded waveguide, which confines the light in two dimensions, by thinking of a strip-loaded waveguide as a set of slab waveguides. For instance, region I and II can be thought of as a substrate-core-cladding and substrate-core-air slab waveguide along the z-axis. Each region has their own optical mode, propagation constant β_{I} and β_{II} and effective index of refraction as determined from the previous section **2.2.1**. Since there is less penetration of the EM-field into the air layer than the cladding layer (Goos–Hänchen effect) [22], the effective index of refraction in the region under the loaded-strip is higher than the propagation constant in the surrounding region. This contrast between regions I and II then forms an effective symmetric slab waveguide in the horizontal (y-axis) direction. In addition, the air-cladding-air interface in the horizontal direction can also be described and modeled by a symmetric slab waveguide. Finally, the different vertical and horizontal regions are stitched together to form a two dimensional structure as shown in Appendix A. To complete the EM-field distribution these independent vertical and horizontal distributions are multiplied with each other according to the following equation,

$$E(y,z) = F_i(z) * G_j(y) \tag{10}$$

where $F_i(z)$ and $G_j(y)$ are the solutions of the EM-field distributions of a slab waveguide along the the vertical and horizontal direction in different regions. The subscripts indicate region I / II for i and crystal / air-cladding-air for j.

This method is compared to two other mode solvers, namely the effective index method solver (EIMS) and the wave matching mode solver (WMMS) from SiIO [23][24]. The working principles of these solvers and why they were chosen as a comparison is supplemented in the Appendix section A. In Table 1 the relative intensity in each layer for different solvers is shown. As can be seen, our solver is agrees well with EIMS and WMMS. Our solver over estimates the relative intensity in the cladding layer by only around 1% with respect to EIMS. However, the relative intensity in the substrate layer is basically identical. With respect to WMMS, our solver underestimates the intensity in the substrate layer by around 3.4%. However, in this case the relative intensity in the cladding layer are nearly identical. The only significant difference between our solver and EIMS, is that the EIMS solution is much more horizontally confined. The electric-field is nearly completely located under the loaded strip, whereas for our solver and WMMS the optical mode also extends outside the loaded strip region, as shown in Figure 7. Furthermore, the shape of the electric-field distribution between our solver and WMMS is nearly identical, which shows that describing the strip-loaded waveguide as a set of slab waveguides is a valid approximation to make.

Table 1: Relative optical intensity distribution per layer for our solver and SiIO online solver.

Waveguide Layer	Our solver	SiIO (EIMS / WMMS) [23][24]
Cladding	1.29 %	(2.47/1.41) %
Core	82.5 %	(81.3/78.9) %
Substrate	16.3 %	(16.2/19.7) %

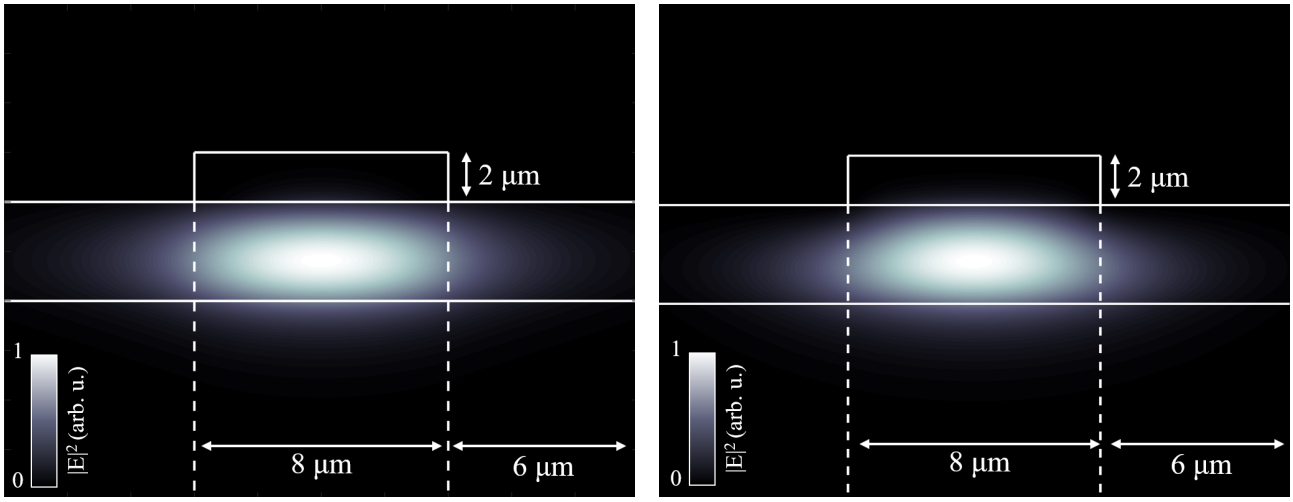

(a) Our solver (b) SiIO WMMS

Figure 7: Intensity distribution ($|E|^2$) of the zeroth order TE mode inside the strip loaded waveguide, with a core and cladding thickness of 4 µm and 2 µm respectively. a) Own solver describing the strip-loaded waveguide as a set of slab waveguides. b) Solution of the WMMS solver.

The advantage of our method with respect to EIM, is that it is able to more accurately describe the EM-field profile. In addition, our method is almost identical to the WMM result, while being

significantly faster. Our solver is able to determine the EM-field profile within a second, while WMM takes around a minute (depending on the parameters set). Furthermore, our method is the closest to being an analytic solution, since it does not use a finite difference method to solve the Helmholtz equation. Instead, only the (effective) refractive indices are used to determine the shape of the EM-field profile. Therefore, it allows a greater understanding of the physics at play. Finally, this method can be extended to any waveguide which is constant along the optical axis and can be described as a set of slab waveguides.

2.3 Types of Losses in Doped Semiconductor Waveguides

The intensity of the EM-wave guided through the waveguide reduces exponentially according to Beer's law, which is also known as attenuation. As was shown before, the distinctive EIT transmission peak at zero detuning is highly dependent on the intensity of the control beam. Therefore, depending on the amount of attenuation, there exists a distance where the intensity of the control beam is too low to effectively drive the system, resulting in the loss of the EIT signal. By categorising all possible types of attenuation and the magnitude of the losses they inflict, we will be able to determine the optimal length of our waveguides. Such that there is still a detectable transmission signal while maintaining as many addressable defects/impurities as possible.

2.3.1 Scattering

In total there are two types of scattering for waveguides. There is volume scattering, which is caused by imperfections like crystalline defects and/or impurities and there is surface scattering, which occurs when the propagating light-wave interacts with the surface. In doped SiC, volume scattering is negligible compared to surface scattering, because the size of the imperfections are small compared to the wavelength [14]. Surface scattering can be described using the ray-optics method. The light-wave reflects from the interfaces and depending on the thickness of the guiding layer the light-wave undergoes N_R amount of reflections over a distance L. For every reflection there is a loss due to surface scattering, depending on the surface roughness. Higher order modes have a larger incident angles and undergo more reflections, resulting in a higher loss than lower order modes. However, in our case absorption losses are much higher, therefore losses due to surface scattering are negligible [14].

2.3.2 Interband Absorption

Via the absorption of a photon, transitions from the valence to the conduction band can occur for semiconductors like SiC. This process is known as interband absorption and has the ability to result in a large attenuation coefficient, on the order of 10^4 cm^{-1} [14]. For these transition to occur it is required that the photon energy is greater than the bandgap energy, which is around 3.26 eV or 380 nm for undoped 4H-SiC [25][26][27]. The wavelengths we use are in the telecom waveband, which are much longer than the wavelengths required for interband absorption. Therefore, in our case the effect of interband absorption is negligible. This also holds true in the case that impurities or dopants are added to the sample, because it shifts the bandgap energy on the order of meV [28][29].

2.3.3 Free-Carrier Absorption

Previously, the effect of carrier concentration, induced via doping, on the real refractive index was discussed. Following from equation (8), these free-carriers also have an influence on the imaginary refractive index $\kappa \equiv \sqrt{\epsilon_2}$, which is associated with optical absorption. Similarly, in the infra-red regime, where $\omega\tau \gg 1$ and $\omega \gg \omega_p$, the attenuation constant α_{fc} is given by [19][14]

$$\alpha_{\text{fc}} = \frac{2\kappa\omega}{c} = \frac{Ne^3}{nc\,\epsilon_0(m^*)^2\mu\,\omega^2}, \tag{11}$$

where we multiply with a factor of two because the intensity of light is proportional to the square of the electric-field, and $\mu = e/\gamma\, m^*$ is the low-field mobility of the free-carriers in the material. The most important parameter in the attenuation constant is the doping concentration N. This is because the other parameters are either constants of nature or are inherent to the material in question, like the index of refraction and the effective mass. In our case the excitation frequency (ω) is also fixed by the range of the telecom waveband. Therefore, the only parameter left to discuss is the mobility of the free-charges. However, the mobility also heavily depends on the doping concentration and doping type. In 4H-SiC the mobility is on the order of 50 to 100 cm^2/Vs for doping concentrations ranging from 10^{18} to 10^{19} cm^{-3} [27][30][31]. On average the mobility of holes is on the order of ten times lower than that of electrons, thus resulting in an approximate ten fold increase in the attenuation constant.

2.3.4 Radiation

Radiative modes are EM-field oscillations outside the guiding layer, which do not exponentially decay like evanescent modes and occur when $n_{\text{eff I}} \leq n_{\text{eff II}}$. For normal guided modes $n_{\text{eff II}} < n_{\text{eff I}} < n_{\text{c}}$, but because $n_{\text{eff II}}$ and $n_{\text{eff I}}$ only differ by a few ten-thousands, any slight disturbance in the EM-field will cause the order to flip and thus result in the radiative modes. The application of curves in waveguides causes such deformation to the EM-field of the guided wave and therefore create radiative modes [14]. Therefore, losses due to radiation become significant in the case of waveguide bends. A way to quantify this effect is the velocity method developed by Marcatili and Miller [32]. For the wave to remain guided it has to maintain a constant phase-front. Since the distance needed to traverse is longer for larger radii, the tangential phase velocity has to be proportional to the distance from the center of the bend to maintain the constant phase-front. Then there exists a radius R + X_r where the phase velocity has to exceed the velocity allowed by the index of refraction in the surrounding region. Beyond this region the phase-front cannot be maintained and the EM-field will split off from the guided mode and converted in radiation. Assuming that the length X_r is larger than half the waveguide width (so that the EM-field only splits off outside the guiding layer) and that the angular velocity has to be equal for all waves along the phase front, the length X_r can be described in the following way

$$X_r = \frac{\beta_{\text{I}} - \beta_{\text{II}}}{\beta_{\text{II}}} R. \tag{12}$$

R is the radius of the bend and β_I and β_{II} are the propagation constants in the confining and surrounding layer respectively [14]. The splitting of the guiding and radiative modes is not immediate. An estimation was given that the radiative mode remains connected to the guiding

mode within the distance Z_c measured along the guided path by,

$$Z_c = \frac{d^2}{2\lambda_{\mathrm{II}}} \tag{13}$$

where d is the thickness of the waveguide and λ_{II} is the wavelength inside the medium surrounding the confining region [14]. Thus, the optical power located further than X_r away from the center of the waveguide bend is lost after a distance Z_c and if $P(z)$ is the power transmitted at a distance z along the optical axis; then the attenuation coefficient related to radiative losses is given by,

$$\alpha_{\mathrm{rad}} = -\frac{1}{P(z)}\frac{dP(z)}{dz} \simeq \frac{1}{P_{\mathrm{tot}}}\frac{P_{z>X_r}}{Z_c} \tag{14}$$

where P_{tot} is the total optical power and $P_{z>X_r}$ the optical power beyond X_r which is lost as radiation. If one knows the EM-field distribution one can determine these powers via integration over the region of said fields. In general, if one assumes that inside the confining layer the field has a sinusoidal form and decays exponentially outside the confining layer, then the attenuation coefficient will decrease exponentially with increasing X_r [14]. From equation (12) it becomes clear that to limit radiative losses one requires a large radius of curvature or a high contrast in index of refraction between the confining and surrounding layer. In our case, because of the low contrast in refractive index along the horizontal y-axis, between the confining (I) and surrounding (II) regions, the losses due to radiation are determined to be on the order of 50 dB/mm in section **4.1**.

2.4 Optical Coupling between Optical Fiber and Waveguide

For light to enter the waveguide, an outside optical source has to be coupled to the waveguide. Previously this was done via the direct focusing of a mounted lens for a slab waveguide [11]. However, to perform future EIT measurements, the sample must be cooled down in a cryostat at around 4K. When the sample is inside the cryostat, optical alignment is extremely difficult. The tolerances to couple light into and out of a waveguide are on the order of micrometers and therefore we wish to align the optical source and waveguide before it enters the cryostat. Therefore, it was decided to use an optical fiber which is aligned to the waveguide using a six-axis stage. Then, in the future, there is the possibility of permanently attaching an optical fiber to the waveguide at both the in- and out-facet of the waveguide such that the waveguide can be put in another environment without having to align the system again.

2.4.1 Butt-coupling

Highly efficient coupling between a parallel optical fiber and waveguide is possible, due to the ability of making the guiding layer thickness around the same size of the optical fiber core. In addition, the optical mode of the optical fiber is closely matched to the TE_{00} mode of a waveguide. As long as the optical fiber is perfectly perpendicularly cleaved, then the optical fiber and waveguide facet can be brought within a few micrometers of each other. Causing further improvements to the mode overlap. In general, the coupling efficiency η between the optical fiber and the waveguide is given by,

$$\eta = \frac{\left|\int \mathcal{E}_o^* \mathcal{E}_c \, dA\right|^2}{\int |\mathcal{E}_o|^2 \, dA \int |\mathcal{E}_c|^2 \, dA} \tag{15}$$

where $\mathcal{E}_o$ and $\mathcal{E}_c$ are the respective complex electromagnetic fields in the optical fiber and waveguide, integrated over an area A [33]. For simplicity, we will only consider one dimension in the following example. The coupling between an optical fiber and our waveguide along the z-axis is shown in Figure 8. When the separation between the optical fiber and waveguide is zero, then the coupling efficiency to a TE_0 mode is as follows,

$$\eta = B \frac{n_o n_c}{(n_o + n_c)^2} \frac{d_c}{d_o} \cos^2\left(\frac{\pi d_c}{2 d_o}\right) \frac{1}{\left[1 - \left(\frac{d_c}{d_o}\right)\right]^2}. \tag{16}$$

Here B is a normalisation constant and n_o and n_c are the indices of refraction of the optical fiber and the waveguide core. The second term in equation (16), related to these refractive indices, describes the reflection between the optical fiber and waveguide facet [33]. Furthermore, d_o and d_c are the thickness of the optical fiber core and waveguide core respectively. Their ratio determines the area mismatch and the final term in the equation represents the mode overlap. A similar description can be made for optical coupling along the y-axis, where the core thickness d_c is replaced by the width of the loaded strip. Equation (16) implies that maximum coupling occurs when the thickness of the optical fiber core and waveguide core layer are the same $d_o = d_c$. Furthermore, the facets of the optical fiber and waveguide act as a semi-transparent mirror. Based on the refractive index of the optical fiber n_o and the waveguide n_c, a portion of the light is reflected. This reduces the transmission of the initial beam, but also the total transmission, due to Fabry-Pérot interference depending on the separation L between the optical fiber and waveguide. This Fabry-Pérot interference is discussed in the next section. These conditions should be taken into account when choosing which optical fiber to couple to the waveguide or what the waveguide dimensions should be during the design process. For instance, our optical fiber has an emitting layer thickness of around 9 µm [34] and our waveguides have widths ranging from 6 to 9 µm. Therefore, it is expected that the loaded strips with a width of 6 µm will have a lower transmission than those with a width of 9 µm, because of the reduced mode overlap.

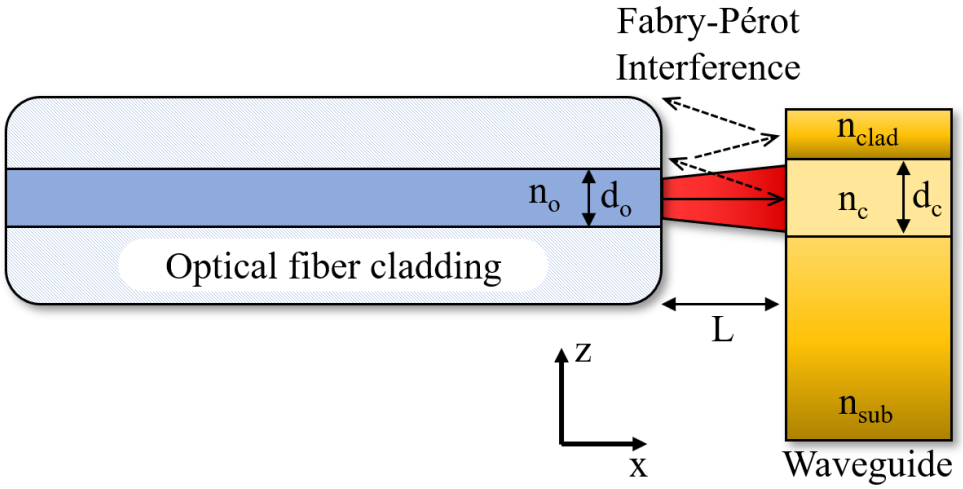

Figure 8: Schematic of butt-coupling between the optical fiber and our strip loaded waveguide, along the z-axis. For maximum coupling efficiency, the optical mode between the fiber and waveguide have to match. For a TE_0 mode, this mode matching mainly depends on the ratio between the thickness of the optical fiber emitting layer d_o and the waveguide core d_c.

2.4.2 Fabry-Pérot Interference

Coupling light from an optical fiber to the waveguide results in the formation of a Fabry-Pérot etalon, as shown in Figure 8. Depending on the separation between the optical fiber and the waveguide (L), successive reflections will interfere constructively or destructively. This can change the total transmission with sub-micron changes in the separation. If one tries to determine the best working waveguide from an array of samples, then this change in total transmission can become a problem. Because, if the gain in transmission between different waveguides is smaller than the effect of Fabry-Pérot interference, then no valid conclusion can be made. Since the change in intensity could also be attributed to the aforementioned effect. The impact of Fabry-Pérot interference can be reduced by including an index matching fluid [35]. However, this reduces the freedom of the optical fiber position, since the fluid will act as weak adhesive between the optical fiber and waveguide. By moving the optical fiber this connection is broken and will cause residue to be left behind on the fiber tip and waveguide facet, which in turn can influence the coupling efficiency and reduce the total transmission.

The total transmission for a parallel-plane Fabry-Pérot etalon is given by,

$$T = \frac{(1 - R_1)(1 - R_2)}{1 - 2\sqrt{R_1 R_2}\cos(\phi) + R_1 R_2} \tag{17}$$

where R_1 and R_2 are the reflectance of the two surfaces and ϕ is the phase difference between each successive transmitted pair [19]. The difference in maximum and minimum transmission can be calculated by taking the absolute difference of equation (17) for the maximum and minimum value of the cosine term,

$$\Delta T = \left| \frac{4(1 - R_1)(1 - R_2)}{(1 + R_1 R_2)^2 - 4\sqrt{R_1 R_2}} \right|. \tag{18}$$

In our case the optical fiber is assumed to be made of fused silica with a reflectance of 3.3% and the SiC waveguide has a reflectance of around 19%, which results in a total transmission difference of $\Delta T \approx 25\%$, as shown in Figure 9.

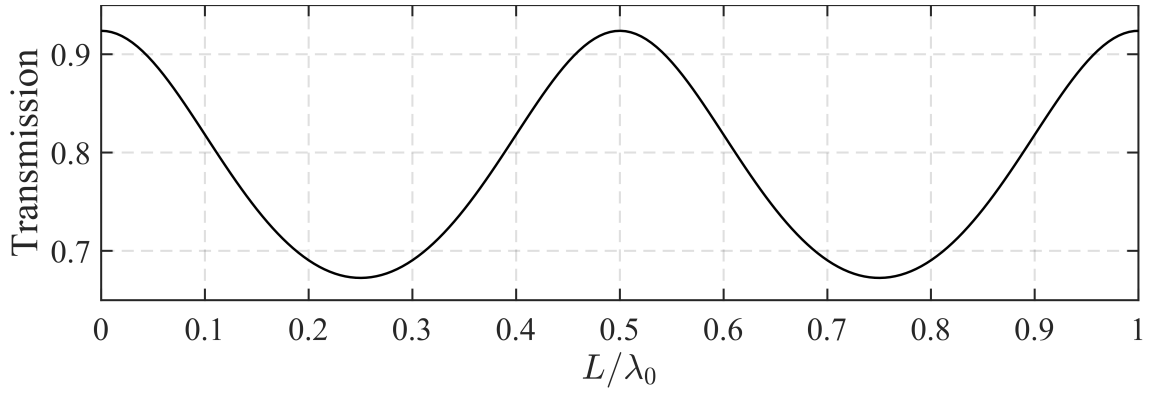

Figure 9: Theoretically expected total transmission oscillations due to Fabry-Pérot interference between the optical fiber tip and waveguide.

The frequency of the oscillations between the maximum and minimum transmission is determined by the phase difference ϕ. This phase difference depends on the length L of the etalon,

the incident angle θ with respect to the surface normal, the vacuum wavelength λ_0 and the index of refraction n of the etalon medium in the following way,

$$\phi = \left(\frac{2\pi}{\lambda_0}\right) 2nL\,\cos(\theta) \tag{19}$$

which can be derived as the difference in pathlength between two successive transmission pairs multiplied by the wavenumber. For maximum transmission to occur the cosine term in equation (17) has to be maximized, which combined with equation (19) states that $2nL\,\cos(\theta)$ must be an integer multiple of the wavelength. In our case we are able to further simplify by setting the index of refraction $n = 1$ and perform the small angle approximation $\cos(\theta) \approx 1$, because the Fabry-Pérot interface medium consists of air and the normal incident angle is small (on the order of a degree). It is therefore expected that in our case the spatial frequency of this Fabry-Pérot interference is approximately $1/L = 2/\lambda_0 = 1.54\,(\mu\text{m})^{-1}$, for $\lambda_0 = 1.3\mu\text{m}$. However, slight deviations are expected from this value due to the 'walk-off' effect, which is caused by our optical fiber and waveguide not being infinite parallel-planes. Therefore, after a couple of reflection the light will leave the etalon. Furthermore, reflections from the optical fiber cladding will influence the interference differently, because this layer does not emit light and has a different refractive index.

3 Experimental Setup

In order to couple light from a optical fiber into the waveguide, a setup as described by Figure 10 is used. A laser with a wavelength of 1.3 µm is coupled into a polarization maintaining fiber patch cable which carries the light to the setup. The fiber patch cable is then coupled to a bare polarization maintaining optical fiber which is situated on a six-axis stage. The waveguide is attached to a holder, which stabilizes the waveguide position and can be used as a future platform to permanently attach the optical fiber to the waveguide. With the assistance of a long working distance objective camera, which is positioned at the side of the sample, the optical fiber is brought to around ten micrometers of the waveguide by the six-axis stage. The transmitted light is collected by an aspheric lens. The collimated light is then directed to a beamsplitter (BS), which directs the light to a photodiode (PD), with a diaphragm in front to block unwanted light, and a CMOS camera. The camera allows us to look at the signal at the end-facet and therefore compare the experimental results to the theoretical field distribution of the waveguide. In addition it is used in combination with the PD to verify the transmission results.

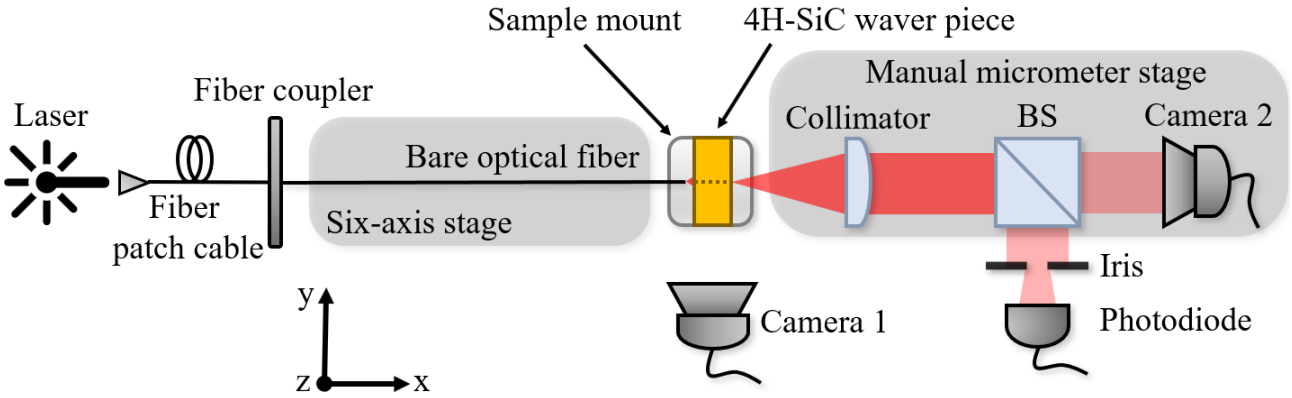

Figure 10: Schematic top view of the experimental setup. Light from a laser is coupled into an optical fiber, which is aligned to the waveguide by a six-axis stage. The transmitted light is collimated and directed to a beamsplitter (BS) which directs the light to a photodiode and CMOS camera. The position of the collimator, BS and camera is changed using a manual micrometer stage in order to focus the transmitted signal.

The six-axis stage allows for sub-micrometer movement in the translational x,y and z-directions and angular rotations around each axis labeled as yaw for the y-axis, pitch for the z-axis and roll for the x-axis. The six-axis stage is driven by a set of stepper motor actuators, which are able to be digitally controlled allowing for higher precision and repeatability of measurements. A limitation that has to be taken into account, is that the six-axis stage is only able to be positioned in steps of 1 µm in the translational directions. Measurements can be taken while the stage is moving, however this is only possible for one direction. Thus, if we scan over two or more dimensions then one will have sub-micrometer resolution, whereas the others will have micrometer resolution. Since the waveguide structures are on the order of a few micrometers, the resolution of the six-axis stage is starting to become a limiting factor for optimal coupling.

3.1 Waveguide structure

The original sample is a square monolithic 4H-SiC wafer piece of around 1 by 1 cm, with multiple loaded strips in the shape of serpentine bends, as shown in Figure 11(a). These bends have four different radii, resulting in length variations of: 0, 1, 2 and 2.5 mm (in addition to a base length of 17.665 mm between the last marker midpoints). The motivation for these different lengths was to more easily determine the losses in the waveguide, by comparing the optical transmission intensity for the different length variations. In addition each bend consisted of seven individual loaded strips with different widths, ranging from 6 to 9 µm with 0.5 µm interval as shown in Figure 11(b). This was done to ensure that in at least one case there would be waveguiding, as there was some uncertainty from previous simulations which width would properly support a zeroth order mode at a wavelength of 1.3 µm. Lastly, the core and cladding layer have a thickness of 4 and 2 µm, respectively.

4H-SiC has a base refractive index of $n = 2.517$ for TE polarization at a wavelength of 1.3 µm [36]. In order to provide a contrast in the index of refraction between the different layers, the substrate and cladding layer are heavily n- and p-type doped respectively. The doping concentrations in question are: $5 \cdot 10^{18}$, $5 \cdot 10^{14}$ and $2 \cdot 10^{19}$ per cubic centimeter for the respective substrate, core and cladding layers. This results in the refractive indices of each layer: $n_{\text{sub}} = 2.5668$, $n_{\text{core}} = 2.5703$ and $n_{\text{clad}} = 2.5613$, as calculated from the change in real refractive index given by equation 9.

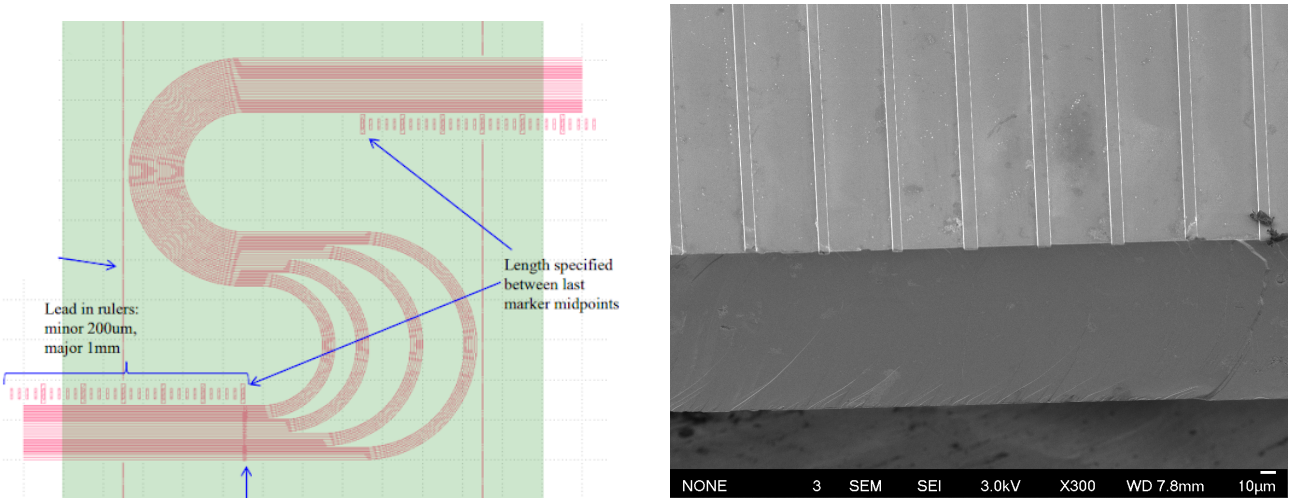

(a) (b)

Figure 11: Structure of monolithic 4H-SiC strip-loaded waveguide. a) Illustration of original sample with serpentine bends of different lengths, where the green square is around 1 by 1 cm b) Scanning electron microscope overview of an array of loaded strip, taken at 40 degrees viewing angle.

3.2 Alignment Protocol

To roughly couple light from the bare optical fiber into the waveguide the following steps are taken. First, the optical fiber is brought to around ten micrometers of the waveguide with the help of a long working distance objective NIR camera located at the side of the sample. Secondly, the position of the collimator, BS and camera is changed using a manual micrometer stage, such that the end facet is brought into focus, as can be seen in Figure 13. Once the end facet is in focus, the optical fiber is moved up along the z-axis such that the light shines over the surface and creates a diffraction pattern. A depiction of this effect is provided in Figure 23 in the appendix section **B**. When the diffraction pattern becomes visible the direction of travel of the optical fiber is slowly reversed, such that higher order diffraction modes vanish. At the moment the final diffraction peak disappears a small optical aberration above the waveguide surface is visible on the camera. This is the transmitted signal, but due to chromatic aberration between IR and optical wavelengths the focus of the transmission signal is not the same as the waveguide end-facet. Therefore the collimator, beamsplitter and camera are realigned with the manual micrometer stage to bring the transmission spot into focus.

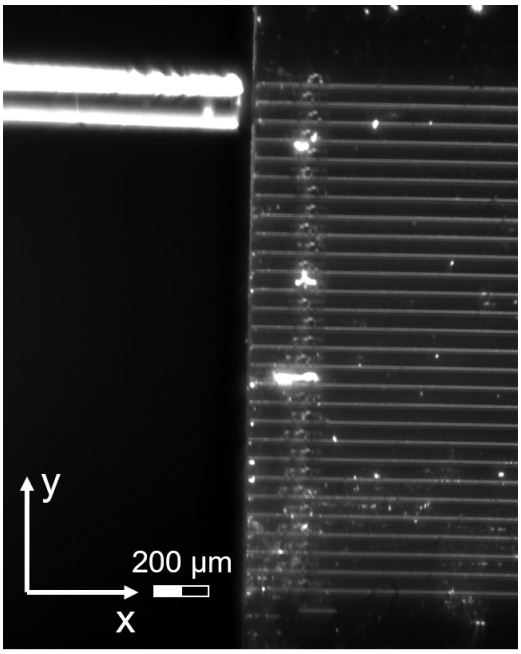

Figure 12: Image taken with camera 1 of the optical fiber (on the left) and the waveguide (on the right) at the in-facet. The total width of the optical fiber is around 130 µm, whereas the emitting layer is only around 9 µm, which makes it difficult to align the optical fiber by eye.

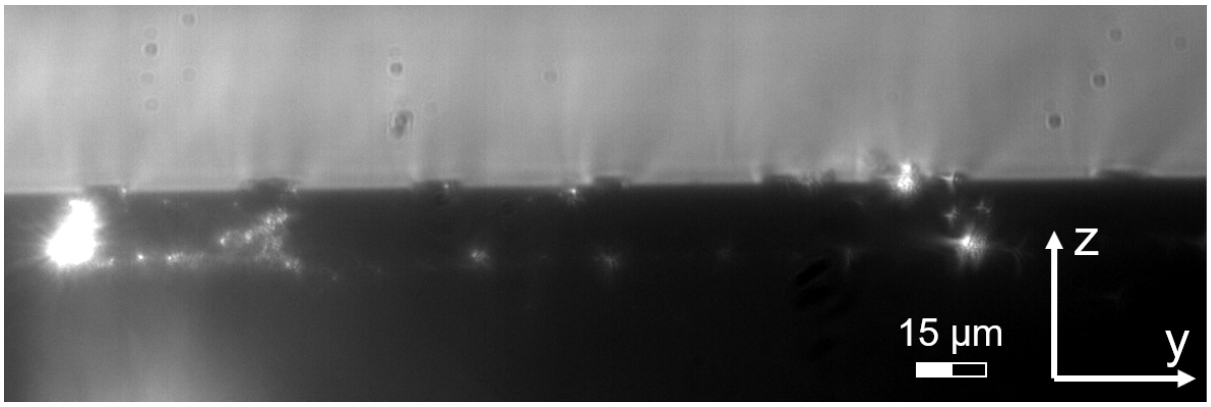

Figure 13: Image taken from the end-facet of the waveguide with camera 2, illuminated using a high intensity fiber optic LED. The array of loaded strips are visible as small rectangles on top of the surface, i.e. at the black to gray interface in the image.

To maximise the coupling efficiency, the translational and angular mismatch between the optical fiber and the waveguide has to be minimised. In order accomplish this we developed a protocol, which should be able to determine the angular mismatch on the order of minutes. In Figure 14 the operating mechanism of the protocol is shown. If there exists an angular

mismatch (α) along the yaw-axis, then by moving the optical fiber along the optical-axis the location of the optical coupling along the y-axis also changes. For small angles the ratio of change in the coupling location along the y-axis (Δy) and the optical-axis (Δx) is equal to the mismatch angle α. Thus, by keeping track of an easily distinguishable point in the signal (for example the point of maximum transmission), one can plot Δy versus Δx and perform a linear fit to determine α. Then by adding or subtracting α to the yaw-axis, depending on the chosen basis, the optical fiber should be perpendicularly aligned to the sample. However, in practice this might prove to be an iterative process, because of non-linearity at larger angles ($\tan(\alpha) \neq \alpha$) and errors/uncertainty during measurement. The process is identically for the pitch-axis, where the displacement along the z-axis is used.

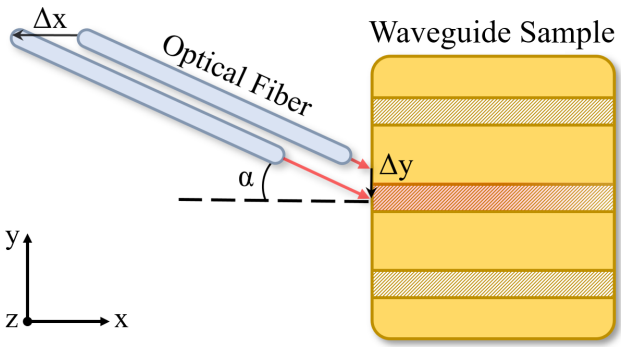

Figure 14: Schematic of the angular misalignment of the optical fiber with respect to the waveguide. Movement of the optical fiber along the optical x-axis changes the coupling location in the y-axis, depending on the angle α.

Finally, for the best optical coupling between the optical fiber and waveguide the separation along the optical axis between the two components has to be as small as possible. With the camera on the side of the waveguide we are able to achieve a separation on the order of ten micrometers. This is due to the fact that the waveguide and optical fiber cannot be in focus at the same time and due to the resolution of the camera. In order to reduce the separation between the optical fiber and the waveguide, the Gaussian beam characteristics of the light leaving the optical fiber is utilized. Namely the optical intensity at a distance x away from the optical fiber tip is given by [37],

$$I = \frac{2P}{\pi w^2(x)} = I_0 \frac{x_R^2}{x_R^2 + (x - x_0)^2} \tag{20}$$

where P is the total power of the light coming out of the optical fiber and $w(x)$ is the radius of the Gaussian beam waist. Then by using the definition of the Rayleigh length x_R, the final expression on the right is determined. Therefore by retracting the optical fiber along the optical axis, as described in the previous paragraph, the intensity measured by the PD should follow equation 20. By performing a best fit the distance between the optical fiber and the waveguide, in terms of the six-axis stage settings, can be determined from the parameter x_0. Care should be taken with regards to Fabry-Pérot interference when performing alignment by moving the optical fiber along the optical axis. As discussed in section **2.4.2**, the optical fiber and waveguide form a Fabry-Pérot etalon which influences the transmission. The period of the oscillations in total transmission is less than 1 µm, while the six-axis stage can only be positioned in 1 µm intervals. In practise we can measure the transmission during the motion from one position to another, which allows for sub-micrometer resolution. However, in the end only 1 µm changes in position can be made. Therefore, the point of maximum transmission cannot be determined exactly. After the alignment protocols have been completed, the coupling of the optical modes between the optical fiber and waveguide should be at a maximum, resulting in the highest transmission intensity at the end-facet of the waveguide.

4 Results and Discussion

The following sections we will present the transmission signal of our waveguide and compare it to the theoretical predictions. Based on the results, it will be argued whether the monolithic SiC strip-loaded waveguide is a suitable platform for future EIT measurements or another design has to be considered. Secondly, the results of the optical alignment protocols will be investigated and we will discuss if they are applicable in future research. Finally, in order to determine the maximum allowed length for a doped waveguide, such that sufficient light is transmitted to perform EIT measurements, the contribution of free-carrier absorption to optical attenuation will be discussed.

4.1 Serpentine Bends and Radiation Losses

At the start of the measurements we wanted to couple light into the waveguide and look at the transmission signal and compare it to the theoretical predictions, to ensure that the waveguide is working properly. However, in our original sample with serpentine style bends there was no detectable transmission signal when looking at the camera image of the end-facet of the waveguide. In addition, the data recorded by the photodiode consisted mainly out of scattering and edge diffraction from the loaded strips. To exclude any problems regarding optical fiber coupling, the optical fiber was briefly replaced by a lens which focused the light on the in-facet, as was done in a previous experiment [11]. However, this did not result in any noticeable change in the transmission measured at the out-facet and we therefore immediately switched back to the optical fiber setup. Upon further investigation we noticed that there was light scattering out of the end-facet but not at the location of the loaded strips. Instead the scattered light was located at the opposite side, at approximately the same height as the loaded strips in the in-facet, which signified the possibility that the light might not have been properly confined and guided through the bends. It is generally known that losses due to radiation might be significant in strip-loaded waveguides with bends due to their relatively low horizontal contrast in index of refraction [14]. Although it was expected that the bends had sufficiently large radii for proper waveguiding, these results prompted for a deeper investigation.

First of all, by using equation (12) from section **2.4.4**, the distance from the center of the waveguide strip where the guided wave couples to radiative modes was determined. According to the effective refractive index method, at a wavelength of 1.3 μm the effective index of refraction is $n_{\mathrm{I}} = 2.5685$ under the loaded strip and $n_{\mathrm{II}} = 2.5679$ in the regions without a strip. Leading to the respective propagation constants $\beta_{\mathrm{I}} = 12.4140\ (\mu\mathrm{m})^{-1}$ and $\beta_{\mathrm{II}} = 12.4114\ (\mu\mathrm{m})^{-1}$. Combined with the approximate bend radius of around 2 mm this resulted in the distance $X_r \approx 0.4$ μm, which is an order of magnitude smaller than the width of the loaded strips. Therefore, even the light guided in the confined layer will leak away as radiation. This results in enormous losses (on the order of a couple of hundred dB/cm). Technically equation (12) only holds if X_r is large enough to not be in the confining region, however this does not affect the conclusion. Because, if X_r is within the confining layer then $\beta_{\mathrm{I}} = \beta_{\mathrm{II}}$, resulting in $X_r = 0$ for any radius. Thus, also in this case the light would not be guided through the bends.

This result is also visualised by using a mode solver for waveguide bends. In Figure 15 the electric-field and intensity distribution are plotted for an optical mode traveling through a bend of radius 2 mm. To have a valid solution the index of refraction in the regions without a loaded strip has been slightly lowered slightly from 2.5679 to 2.5660, because otherwise the SiIO BendS solver would return *"No guided modes found"* [38]. In Figure 15 the coupling to the radiative modes is visible via the increasing in amplitude oscillations of the electric-field outside the loaded-strip region. This results in an exponential increase of the intensity outside the confining region. In the case of Figure 15 the calculated losses are on the order of 54 dB/mm, but in reality this value is even higher; because the contrast in index of refraction between the confining and surrounding layer is even lower than in the simulation. Therefore we can conclude that in our case almost all of the light coupled inside the waveguide leaks away at the bends and thus explains why there was no observed transmission at the end-facet of the waveguide. To remedy this problem, the waveguide sample was diced along the center, creating two straight pieces of waveguides of length roughly 4 and 6 mm as seen in Figure16. After dicing, the facets of both pieces where polished to optical quality. With these new samples optical waveguide transmission at the end-facet was observed almost instantaneously and all following results will be from these diced waveguides.

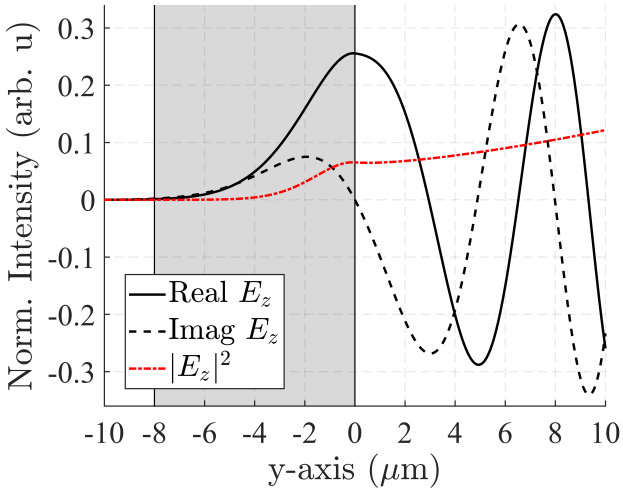

Figure 15: Electric-field and intensity distribution along the y-axis of the waveguide in a bend of radius 2000 µm according to the SiIO online solver BendS [38]. The gray shaded area signifies the region under the loaded strip and positive y-axis values denote the outside region of the bend. The plot is generated by adding the electric-fields throughout the bend. This causes the exponential increase for $y > 0$, because at every step more light escapes as radiation.

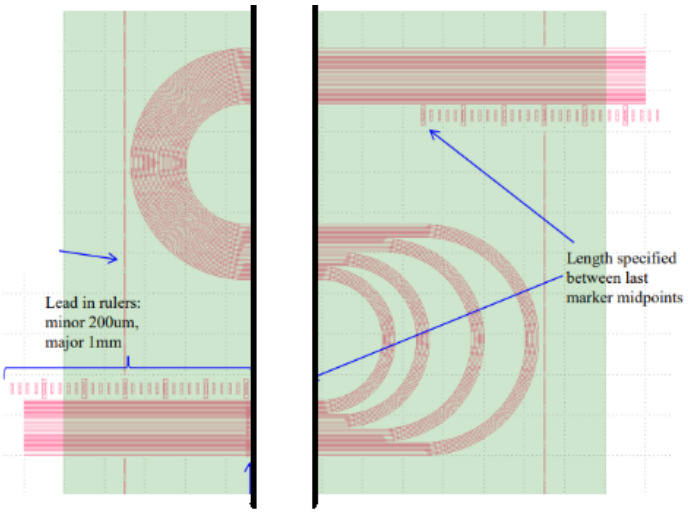

Figure 16: Illustration of the dicing of the waveguide, where the waveguide is split into two parts along the center.

4.2 Observation of Multi-modes and Weak Confinement

After the removal of the bends via dicing a transmission signal was quickly observed. However, the observed signal did not match our theoretical predictions. Namely, optical guided modes were also observed in between the loaded strips, which according to the effective refractive index method should not be possible. In addition, the maximum intensity of the transmitted light in between the loaded strips is around double than that of the intensity under the loaded strips. If only a photodiode was used to detect the transmitted signal, then there would exists a serious possibility of wrongly assigning these higher transmissions to waveguiding under the loaded strip, as this would be expected from theory. Therefore, the inclusion of a camera image of the end-facet of the waveguide is paramount, because it clearly shows where the light is transmitted in the waveguide. In Figure 17 the transmission at the end-facet of the waveguide, when coupling in light at different positions, as seen from the camera, is shown. To properly see the results, the intensity of Figure 17(a) and Figure 17(b) have been amplified by around a factor of ten. Therefore, the results should not be taken as exact but more as an indication of how the optical modes look like.

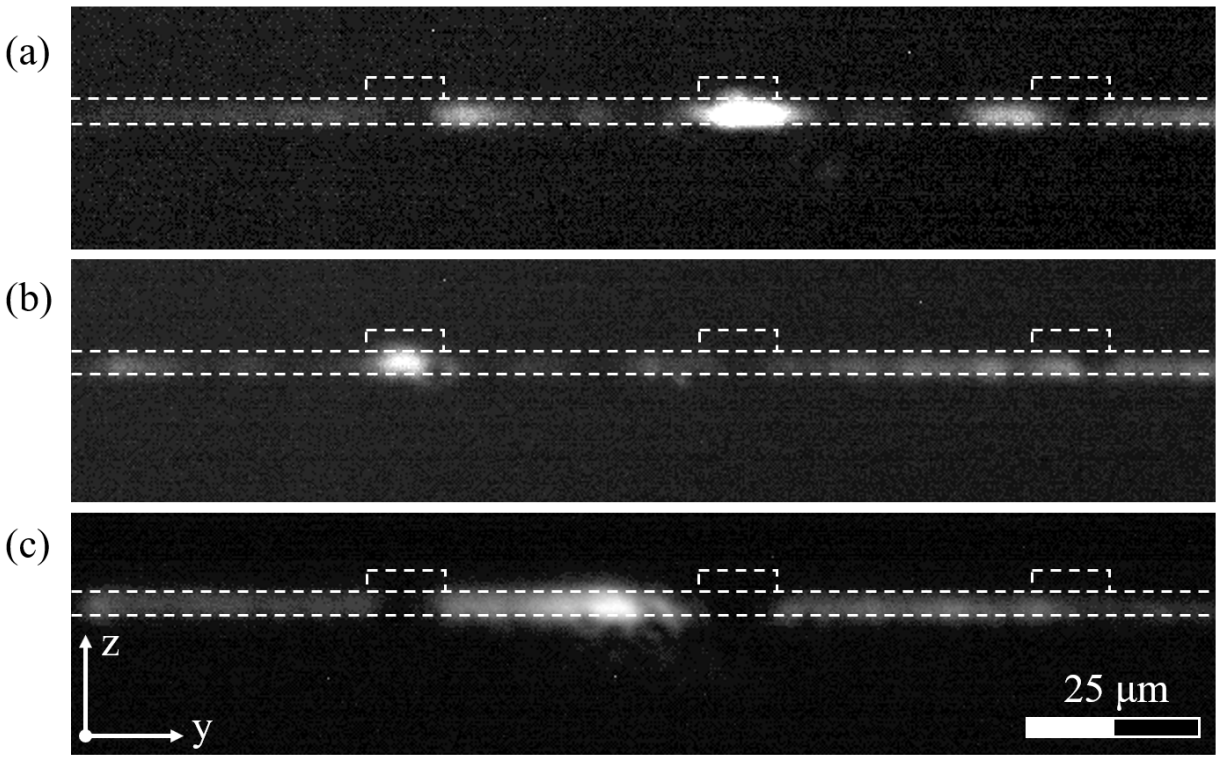

Figure 17: Aligned transmission images at the end-facet of the waveguide as captured by camera 2. Dashed white lines are drawn over the image, to indicate the approximate location of the waveguide structures. (a) Optical mode under a loaded strip. (b) Optical mode under loaded strip neighbouring the strip from (a). (c) Wide optical mode visible in between two loaded strips. Intensity of images (a) and (b) are amplified by around a factor of ten with respect to (c), for clearer graphical comparison.

In Figure 17(a) the light is coupled in, under a loaded strip and has a shape similar as predicted in Figure 7. A small difference is that in reality we measure the intensity while in the theory the electric-field is given, but this only impacts the size and not the shape of the mode. A more

important observation is that there exists leakage, with regular structure, into the neighbouring regions and the light is not completely confided under the loaded strip. The same leakage also occurs for a neighbouring strip as depicted in Figure 17(b), therefore it is not related to a specific defect for one of the strips. Finally, in Figure 17(c) the unexpected mode in between the waveguides can be seen. This mode is relatively well contained and does not enter the region under the loaded strips, as visible from the dark bands, which coincide with the transmission in Figure 17(b) and 17(c).

Due to the discrepancies between the theoretical models and experimental observations, the EigenMode Expansion (EME) solver of Ansys Lumerical was used in order to better understand the observations. The EME method solves Maxwell's equation in the frequency domain and is designed for solving the optical propagation over long distances, because of better scaling than Finite-Difference Time-Domain methods. The method of EME splits the propagation direction into several layers. At the boundary between two layers a mode solution is found using the Finite Difference Eigenmode (FDE) solver. By stitching all the solutions together, along the propagation direction, the propagation of the light is simulated [39]. In Figure 18 the simulated logarithmic intensity of an optical mode propagating through a strip-loaded waveguide with our sample characteristics is shown.

When the optical fiber is perfectly aligned in the center of the loaded strip, as shown in Figure 18(a), most of the light remains confined under the strip. However, there is also a significant amount of divergence visible, which causes some of the light to exists in between the region of loaded strips. This result is most similar to the experimental observation shown in Figure 17(a) and Figure 17(b). In case of a slight misalignment, where the coupling does not occur in the center of the loaded strip, major divergences as depicted in Figure 18(b) occur. This result signifies the importance of aligning the optical fiber as small deviations can significantly reduce the performance of waveguiding. Finally, in Figure 18(c), light is coupled in between the waveguides. In these cases, the light remains largely in confined to this region and does not enter under the loaded strip, as signified by the blue color. This solution represents the observations in Figure 17(c), where the two dark bands coincide with the location of the loaded strips. Yet, there is still one major discrepancy between the experimental results and simulation. Namely, that the predicted intensity, under the loaded strip, is ten times higher than observed. So far, a complete explanation for this still eludes us. But one possible explanation could be that the lower observed intensity is due to the influence of coupling losses. The simulation does not take into account any coupling mechanism or losses attributed to them. Whereas in the experiment the optical fiber is most likely not perfectly aligned and does not couple 100% of the intensity in the waveguide.

Based on these results it becomes clear that the Lumerical EME solver is better at explaining the experimental observations than our solver or WMMS. This is most likely due to the fact that the contrast in refractive indices is too small, such that the assumptions made in the effective refractive index method no longer hold. Another important remark to make is that the boundary conditions of a waveguide simulation are extremely important. Namely, without periodic boundary conditions, Lumerical would not predict the existence of modes outside the strip region. However, when period boundary conditions are selected, or in this case three loaded strips are simulated, then these modes would be predicted. Therefore, the interaction between two loaded strips plays an important role in the experimental observations.

Thus, we conclude that monolithic strip-loaded waveguides with dopants are not a suitable option for confining light over a distance of a few millimeters, as required for enhanced EIT control. The contrast in refractive index from doping is not significant enough to contain the light under the loaded strip in the horizontal direction, resulting in leakage to the surrounding regions. In addition, the inclusion of bends are a requirement for complex photonic integrated circuits [40], which we have also shown to be unfeasible with our strip-loaded waveguide.

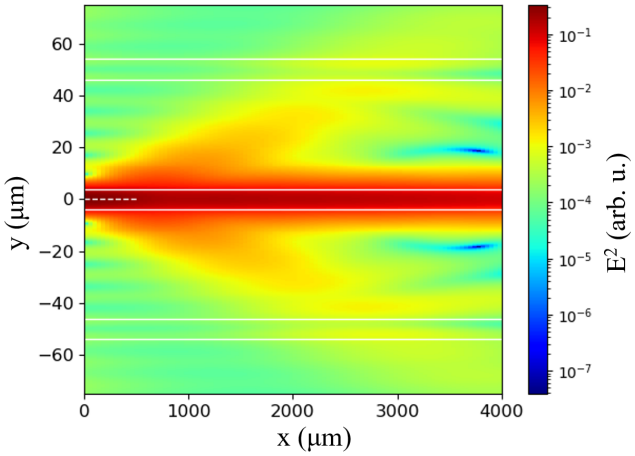

(a) Input source at $y = 0$ μm

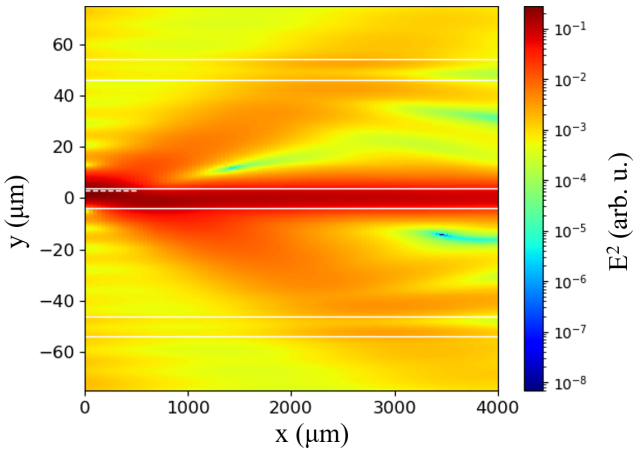

(b) Input source at $y = 3$ μm

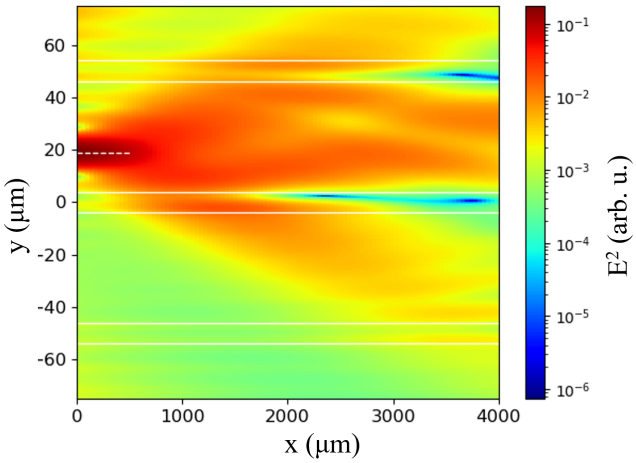

(c) Input source at $y = 19$ μm

Figure 18: Logarithmic electric-field squared $|E|^2$, as the mode propagates in our strip-loaded waveguide, for different input source locations according to Ansys-Lumerical EME solver. (a) Coupling light exactly in the center of the strip causes the majority of the light to be guided. (b) Slight misalignments in the coupling location, on the order of a few micrometers, can cause major divergences and leakages into other regions. (c) Coupling in between the loaded strips causes the light to be confined and propagate in the region in between two loaded strips.

4.3 Model to Determine Losses due to Free-Carrier Absorption

The inclusion of doping in the cladding and substrate layers lowers the real part of refractive index, allowing for optical guiding in the core layer of our monolithic SiC waveguide. However, it also induces significant free-carrier absorption as discussed in section **2.3.3**, due to the high doping concentrations. Following equation (11) the attenuation constant can be determined for each layer depending on the doping concentration and doping type (positive or negative). In Table 2, the attenuation coefficient is given for a p-i-n and n-i-n (cladding-core-substrate) doping structure, with the concentrations as discussed before in section **3.1**. It becomes clear that the highest attenuation occurs at the layers with the highest doping concentration. Furthermore, in this case n-type doping results in a slightly higher attenuation than p-type doping, even though the mobility of of holes with respect to electrons is lower in 4H-SiC [27]. This is due to the fact that the effective mass of holes is smaller than that of electrons, which according to equation (11) results in a lower attenuation coefficient.

Table 2: Free-carrier absorption in different layers of the strip-loaded 4H-SiC waveguide, at an excitation wavelength of 1.3 µm.

Waveguide Layer	α_{fc} (cm^{-1})
Cladding p/n	45.6 / 56.6
Core	0.001
Substrate	8.66

Even though the attenuation per layer has been determined, the question still remains how the system as a whole will act. In experiments the light is simply coupled into the waveguide and the total transmission at the end-facet of the waveguide is being detected. Therefore a system where one converts the attenuation per layer to a type of total loss had to be created. The relatively simple method developed involved multiplying the attenuation constant in each layer by the relative optical intensity in said layer. This method relies on the assumption that regions of high optical intensity will have more interactions with the free-carriers than regions with low optical intensity and will therefore have a higher impact on the system as a whole. By summing over all different layers, an equation for the total loss associated with free-carrier absorption was constructed,

$$\mathcal{L}\mathrm{oss}\,(\mathrm{dB/cm}) = \frac{10}{\ln(10)} \sum_{i}^{\text{all layers}} \alpha_i \cdot I_i^{\mathrm{rel}} \tag{21}$$

where α_i and I_i^{rel} are the respective attenuation constant and the relative optical intensity in a specific layer. Finally, the sum is multiplied by the constant $10/\ln(10) \approx 4.343$ to convert the attenuation to decibels. To check the validity of this equation, it was compared to the PlasS solver from SiIO [41]. This solver determines the losses in a waveguide according to the real and imaginary refractive index. However, PlasS is only able to do this in one dimension. It can therefore not be used for our strip-loaded waveguide. Instead, the losses in a slab waveguide were calculated using equation (21) with the relative intensities from our solver and WMMS. These results are then compared to the results from the PlasS solver and shown in Table 4 in the appendix **C.1** The results that use equation (21) are nearly identical to the result from the

PlasS solver. Therefore, we conclude that this equation is a valid method to calculate the losses in a slab waveguide. Assuming that this method can also be extended to other waveguides that are constant along the optical-axis, equation (21) is used to calculate the free-carrier absorption in our strip-loaded waveguide. The attenuation coefficients per layer are known from Table 2 and the relative optical intensity per layer are in Table 1 from section **2.2.4**. By inserting these values in equation (21), the losses due to free-carriers in a strip-loaded waveguide are shown in Table 3.

Table 3: Free-carrier absorption losses in a (p-i-n / n-i-n) strip-loaded waveguide for the TE_{00} mode, following from equation (21).

Method	$\mathcal{L}$oss (dB/cm) p-i-n	$\mathcal{L}$oss (dB/cm) n-i-n
Our solver	8.7	9.3
EIMS/WMMS	11.0 / 10.2	12.2 / 10.9

For both cases, the expected free-carrier losses are on the order of 10 dB/cm. These losses are large compared to other photonic based circuits using SiC, which can have losses on the order of 0.15 dB/cm [42]. In the case of photonic circuits using silicon nitride, the losses can be as low as 1 dB/m [43]. The reduction in intensity influences the EIT signal, as shown prior in Figure 3, preventing EIT to reach full transparency. Thus, our waveguide should not be longer than a few millimeters (1 to 3 mm). Our solver returns slightly lower losses than EIMS and WMMS, due to underestimating the relative intensity in the substrate layer by around 3%. However, the order of magnitude is still around 10 dB/cm. This is also the same order of magnitude given by a simulation using Ansys Lumerical and agrees with the range of losses observed experimentally [11]. Therefore equation (21) is a valid way to determine the magnitude of free-carrier absorption.

4.4 Future Waveguide Design

For future endeavours a new waveguide type, with a higher horizontal confinement has to be developed. The waveguide can still be made from monolithic SiC, to minimise stresses in the crystal to limit the effects of inhomogeneous broadening. Therefore, doping will still be the method of creating a contrast in the index of refraction of the different substrate, core and cladding layers. To improve the horizontal confinement, the strip-loaded waveguide can be replaced by a rib waveguide, as depicted in Figure 19(a). The core region originally under the cladding layer (I) is raised and the core layer as a whole is made thinner, such that no optical modes are allowed in the core layer of the regions beside the raised edge (II). Due to the raised core layer, the electric-field is located higher in the core layer and the air boundary is used to confine the optical mode in the horizontal direction. This simple modification allows for a significantly higher horizontal confinement, because of to the high contrast in refractive index between the core layer and air. In addition, a small cladding layer can be grown on top of the raised core region, similarly to the strip-loaded waveguide, in order to facilitate a p-i-n style junction for future applications. Furthermore, the losses due to free-carriers are almost identical to that of the strip-loaded waveguide. This is because the horizontal confinement in the core layer does not contribute as much as the cladding layers, due to the doping concentration in the core being four orders of magnitude lower. On the other hand, the increased height of the rib structure (compared to the loaded strip) will increase scattering losses, due to surface

imperfections. However, since free-carrier losses are already around 10 dB/cm, the addition of scattering losses on the order of 1 to 2 dB/cm are not a big factor.

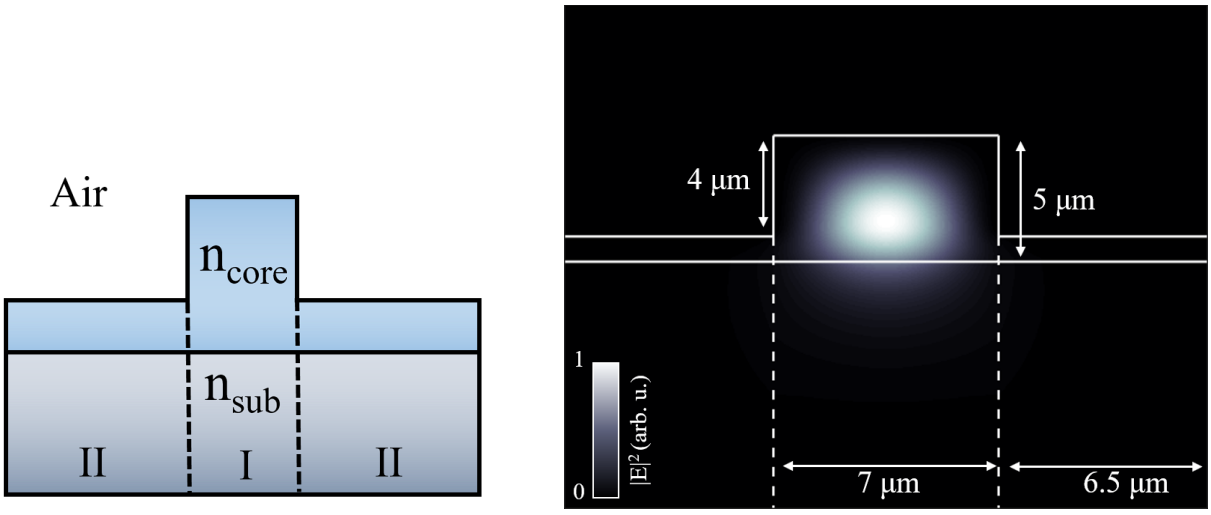

(a) (b)

Figure 19: Future rib waveguide design. (a) Schematic of the rib waveguide structure, where in region (I) the core layer has been raised with respect to the strip-loaded waveguide. (b) Intensity distribution $|E|^2$ of the rib waveguide.

4.5 Optical Fiber Alignment to Waveguide

Although the strip-loaded waveguide is not a suitable platform for enhanced EIT control, due to the low confinement of the optical modes, there still is a visible transmission signal under various loaded strips. This transmission signal can still be used to maximise the mode overlap between the optical fiber and the waveguide. Alignment along the transverse y- and z-axis is relatively simple. Once a rough alignment has been achieved, such that there is some transmission underneath the strip of the waveguide, the optical fiber is scanned along the y- and z-axis until a point of maximum transmission has been found. The angular alignment of the yaw and pitch axis are more difficult to perform, because changing the yaw and pitch angles also changes the transverse alignment. A brute force method would be to simply scan over all possible yaw, pitch, y and z directions, but this would take several hours. Instead, the angular alignment method as described in section **3.2**, where one simply retracts the optical fiber along the x-axis and measures the change in maximum intensity in the y- and z-axis, is tested. Finally, a similar method of retracting the optical fiber along the x-axis, will be used to determine the separation between the optical fiber and waveguide. To maximise the mode overlap and therefore the transmission, the separation between the optical fiber and waveguide has to be minimal. However, care should be taken as to not crash the optical fiber tip into the waveguide sample, as it could damage the optical fiber and/or the waveguide. Based on the results, these methods can be further optimized and be applied to future research, for example the proposed rib waveguide.

4.5.1 Angular Alignment Method

To start off, the optical fiber was brought in alignment along the y- and z-axis, after which the angular alignment method was used to reduce the misalignment along the pitch-axis. (It must

be said that for the following data the sample was mounted differently than shown in Figure 10, in a way that the yaw axis is connected to the z direction and not the pitch. However, for sake of simplicity this change will be omitted and we will keep the basis as defined in section **3**). In Figure 20(a) the result after a single iteration is shown.
From this figure we see that the initial pitch offset is around 2.8°. For optimal coupling we

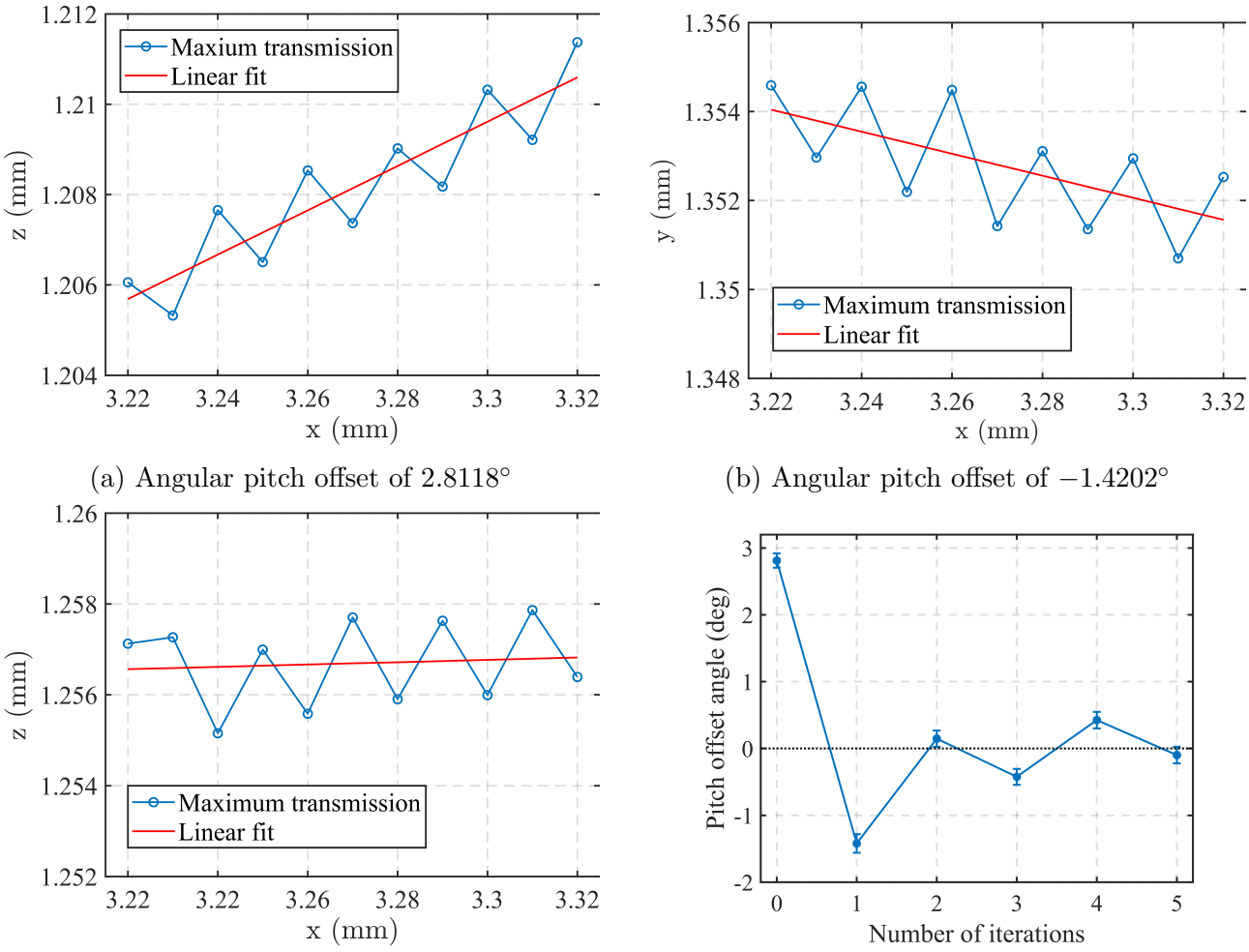

(a) Angular pitch offset of 2.8118°

(b) Angular pitch offset of −1.4202°

(c) Angular pitch offset of 0.1472°

(d) Change in pitch offset angle per iteration

Figure 20: Three iterations of the angular alignment protocol for the pitch axis, as described in section **3.2**, where the slope value is the offset angle. Each data point is the maximum transmission of a z,x scan, as measured from the photodiode. The raw data of one such measurement is shown in Figure 25 in the appendix section **C.3**. The oscillations between successive data points are caused by the six-axis stage, because the motion between the up-down and/or left-right direction differ by around 1 µm. To show the reduction in the slope between iterations, all the y-axis length are constant at 8 µm. (a) Original starting offset, where the method has not yet been applied. (b) First application of the angular alignment method, which reduces the absolute offset by around 1.4 degrees. (c) Second iteration, resulting in a nearly perfect alignment. (d) Change of the pitch offset angle over six iterations.

wish to bring this down to 0°. By subtracting this value from the initial pitch value, the results in Figure 20(b) is obtained. This time the misalignment is in the opposite direction, but the absolute value of the misalignment has reduced. By adding the pitch offset value to the pitch

and performing one more iteration of the alignment method, we got the result in Figure 20(c). As can be seen we have successfully reduced the pitch misalignment to almost 0°. However, further improvements cannot be made due to the uncertainty of the results. When performing several more iterations, the pitch offset keeps changing on the order of ±0.5°. In this case each iteration took around 3 minutes, therefore it took less than 10 minutes to align the pitch axis, whereas a brute force method can take up to an hour.

Unfortunately, the angular alignment method did not work for the in-plane (yaw) axis. At every point in the iteration the offset angle would remain constant, even when moving the yaw along its complete range of motion of 6°. This problem could arise from the weak confinement in the y-axis of the waveguide, but at this moment this is not certain. Future investigations are required to better understand this problem. However, the angular alignment method did work for the combination of the pitch- and z-axis, based on the data in Figure 20 and observation by eye. Therefore, the angular alignment method has some validity behind it.

4.5.2 Optical-axis Alignment and Observed Fabry-Pérot Interference

After the optical fiber was as good as possible aligned, in the transverse and angular directions, only the longitudinal alignment was left to be optimised. To achieve the highest mode overlap and thus maximum coupling, the optical fiber has to be brought as close as possible to the waveguide facet. With the help of the camera at the side of the waveguide, this can be done for a separation of around 10 µm. However, since the optical fiber and waveguide cannot be in focus at the same time, it is impossible to improve this further with just the camera image. According to the method laid out in section **3.2**, the optical fiber was retracted along the x-axis, which caused the transmission to oscillate and decrease as can be seen in Figure 21. In this figure the transmission is plotted versus the relative optical-axis separation, where the zero point of the relative separation is chosen to be the starting point of the measurement as the exact separation can not be known. For the envelope of the data a best fit is made according to equation (20), which gives a Rayleigh length of $x_R = (19.7 \pm 0.3)$ µm and absolute zero-point of $x_0 = (-2.3 \pm 0.4)$ µm. This absolute zero-point basically states that the optical fiber could have been brought 2.3 µm closer to the waveguide. Furthermore, the Raylegh length tells something about how light diverges as it is emitted from the optical fiber. From the divergence angle the numerical aperture (NA) can be determined and compared to manufacturer specification. In the par-axial case, the half divergence angle (θ) is given by [44]

$$\theta = \lim_{x\to\infty} \frac{w(x)}{x} = \frac{w_0}{x_R} = \sqrt{\frac{\lambda_0}{\pi n x_R}}. \tag{22}$$

The NA of the optical fiber is then $\mathrm{NA} = n\sin(\theta) \approx n\,\theta$. In our case, the measured NA is determined to be 0.145, whereas the expected NA from the manufacturer is 0.12. These values are nearly identical and the small increase in NA is most likely due to the fact that we measure the signal through the interaction with a waveguide and not directly from the optical fiber. In the case that the NA was significantly different, like an order of magnitude, then it might indicate non-perfect cleaving, damage and/or dust on the optical fiber tip.

The second observation from Figure 21 are oscillations in transmission intensity as the separation between the optical fiber and waveguide changes. This is indicative of Fabry-Pérot interference as the space between the optical fiber and waveguide mimics that of an etalon.

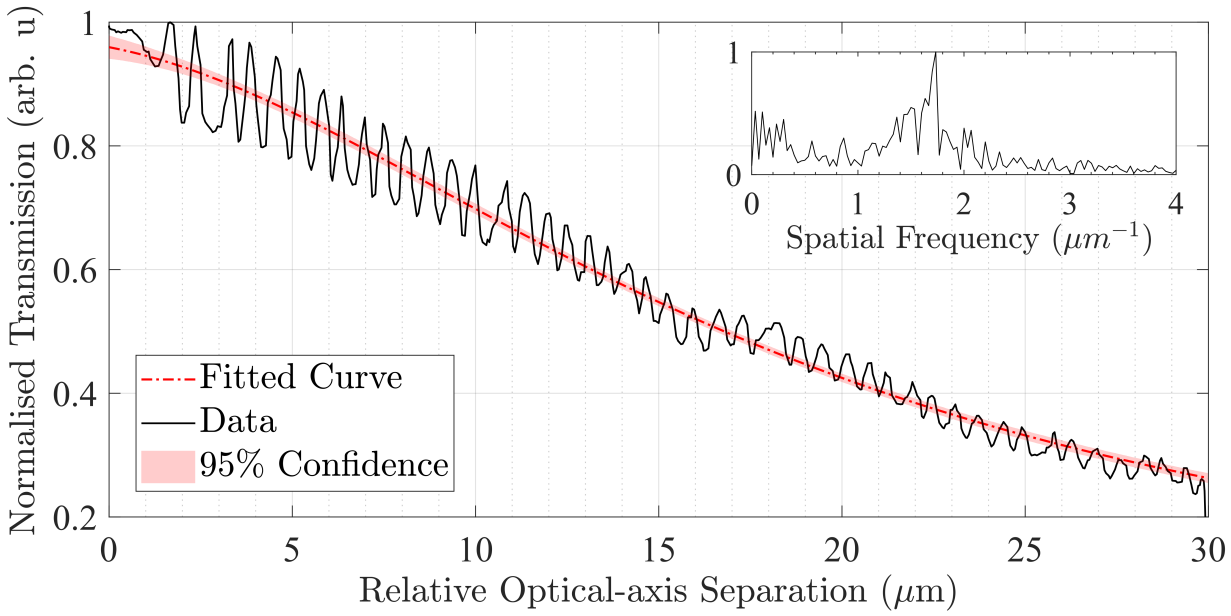

Figure 21: The effect of Fabry-Pérot interference when changing the separation along the optical axis between the waveguide and optical fiber, with its Fourier transform (top right). The fitted Lorentzian function, given by equation (20), describes the envelope of the data. The Rayleigh length determined from the fit is $x_R = 19.7$ µm and the absolute zero-point is located at $x_0 = -2.3$ µm.

However, the exact frequency and transmission difference have to be determined, to exclude the possibility that the oscillations are simply vibrations from the six-axis stage. The frequency of the oscillations are determined by first removing the envelope, via dividing the data by the previous best fit, followed by a Fourier transform. The Fourier spectrum is plotted in the top right of Figure 21 and shows a maximum at 1.73 $(\mu\text{m})^{-1}$, with a standard deviation of around 0.2 $(\mu\text{m})^{-1}$. From theory we expected the oscillation frequency to be 1.54 $(\mu\text{m})^{-1}$, which is not the exact value measured but it is within one standard deviation. Furthermore, the expected change in transmission intensity was determined to be around 25%, which is significantly higher than the measured difference of around $(15 \pm 1)\%$ for separations smaller than 5 µm. However, this can be explained by the fact that our setup is not an ideal etalon. The optical fiber core only has a diameter of less than (9.3 ± 0.5) µm [34] and the surrounding layers are stripped to around 60 µm (or sometimes 125 µm). Therefore, the amount of reflections are limited due to walk-off, especially if the optical fiber is not cleaved completely straight. Furthermore, at larger separations not all of the light is efficiently coupled to the waveguide, because the divergence is larger than the waveguide structures and optical modes. We should therefore model this as light passing through an aperture. For a circular aperture with radius R, the intensity passing through the aperture is given by [44],

$$I(x) \propto \int_0^R r e^{-2r^2/w^2(x)} dr \propto (1 - e^{-2R^2/w^2(x)}). \tag{23}$$

This effect becomes important to consider when the beam radius at location x becomes larger than the aperture radius $w(x) > R$. As an example, if $R = 3\,\mu$m (which is comparable to half the width of a loaded strip), then $w(x) > R$ occurs when the separation (x) is larger than 6.5 µm. This is a small distance, compared to the total distance of 30 µm used in Figure 21.

Therefore, in the future, we should investigate this effect further and look at how it influences the fitting of equation (20) and the calculation of the Rayleigh length.

However, the measured 15% change in transmission over a distance smaller than 1 μm is still significant. If one were to measure different types of waveguides, in order to determine which type would yield the highest transmission, if the difference in transmission is less than 15%, then no valid conclusion can be made. This is because it would be impossible to distinguish between actual data or the effect of Fabry-Pérot interference.

5 Conclusion

The application of EIT in SiC is a serious candidate for use in quantum memory for quantum repeaters, because of long coherence times and emission close to telecom wavelengths. In addition, the mature SiC manufacturing industry allows for the construction of photonic circuits, which allow for greater optical control. However, maintaining sufficient EIT in bulk materials remains difficult due to inhomogeneous broadening due to stresses and inhomogeneities. Previous experiments regarding monolithic SiC slab waveguides showed promise in the enhanced confinement of light. This thesis is a continuation, as monolithic 4H-SiC strip-loaded were analysed as future platforms for enhanced EIT control, because of their ability to confine light in two dimensions instead of one. However, as shown, the strip-loaded waveguides lacked horizontal confinement due to the low contrast in effective refractive index. For the same reason, bends are not supported for this type of waveguide, which severely limits the application of complex photonic circuits. Furthermore, free-carrier absorption plays a significant role in the losses of waveguides where the cladding relies on adding dopants. These losses have been theoretically determined to be around 10 dB/cm and agree with previous experimental results. This means that the use of these waveguides is limited to chip based applications. Therefore, we have concluded that monolithic strip-loaded waveguides are not a suitable platform for future enhanced EIT control.

Finally, several optical fiber alignment methods were discussed. The alignment of optical fibers are an important subject, because it allows for future attachment of the optical fiber to the waveguide, such that the system does not need to be aligned in a cryostat. It was shown that the pitch offset can be reduced to within 1°, but not in case of the yaw-axis. This is most likely due to the low confinement in the y-axis of the waveguide, but more investigation has to be done. We were also able to determine the separation between the optical fiber and waveguide to a few micrometers, which allows for improved coupling due to improved mode overlap. In addition, the Fabry-Pérot interference was observed. This interference resulted in oscillations in the transmission observed, with an amplitude of around $(15\pm1)\%$, when the separation between the optical fiber waveguide was less than 5 μm. The period of these oscillations are smaller than the final position step-size of the six-axis stage. We have circumvent this problem by measuring while the six-axis stage was moving. However, it does mean that we have to be careful when experimenting on multiple types of waveguides. As an example, for multiple waveguides with different widths it will be difficult to know if changes in the observed transmission are due to Fabry-Pérot interference or due to the different geometries of the waveguides.

5.1 Summary of Main Contributions and Future Outlook

The main contributions provided in this thesis are the discovery that doped monolithic strip-loaded waveguides are not a suitable platform for future EIT research, due to their low horizontal confinement. Furthermore, the waveguide solver developed in our group has been improved from being able to solve one dimensional systems into two dimensions, as required for a strip-loaded waveguide. With this addition, losses due to free-carrier absorption have been theoretically determined to be around 10 dB/cm. This value has been found to be similar for the slab, strip-loaded and rib waveguides. Finally, several methods have been developed to aid in the alignment of an optical fiber for future attachment to the waveguide.
In the near future attempts will be made to attach an optical fiber to the waveguide, with the help of the developed alignment methods. Once the optical fiber is attached to the waveguide,

it should be put in a bath of liquid nitrogen. Such that the rough bond strength and thermal displacement between the optical fiber and waveguide can be determined. Furthermore, the rib waveguide proposed for future research is in development and should improve many of the problems associated with the low confinement in the strip-loaded waveguide. If these rib waveguides prove to be successful in confining the light in two dimension, then EIT type measurements can be performed on the divacancies located inside the waveguide.

Bibliography

[1] S. S. Gill, A. Kumar, H. Singh, M. Singh, K. Kaur, M. Usman, and R. Buyya, "Quantum computing: A taxonomy, systematic review and future directions," *Software: Practice and Experience*, vol. 52, no. 1, pp. 66–114, 2022.

[2] G. Alagic, A. Broadbent, B. Fefferman, T. Gagliardoni, C. Schaffner, and M. St. Jules, "Computational security of quantum encryption," in *Information Theoretic Security: 9th International Conference, ICITS 2016, Tacoma, WA, USA, August 9-12, 2016, Revised Selected Papers 9*, pp. 47–71, Springer, 2016.

[3] E. Yablonovitch, H. Jiang, H. Kosaka, H. D. Robinson, D. S. Rao, and T. Szkopek, "Optoelectronic quantum telecommunications based on spins in semiconductors," *Proceedings of the IEEE*, vol. 91, no. 5, pp. 761–780, 2003.

[4] S. Jenkins, D. Matsukevich, T. Chanelière, S.-Y. Lan, T. Kennedy, and A. Kuzmich, "Quantum telecommunication with atomic ensembles," *JOSA B*, vol. 24, no. 2, pp. 316–323, 2007.

[5] A. I. Lvovsky, B. C. Sanders, and W. Tittel, "Optical quantum memory," *Nature photonics*, vol. 3, no. 12, pp. 706–714, 2009.

[6] L. Ma, O. Slattery, P. Kuo, and X. Tang, "Eit quantum memory with cs atomic vapor for quantum communication," in *Quantum Communications and Quantum Imaging XIII*, vol. 9615, pp. 48–55, SPIE, 2015.

[7] V. Yudin, A. Taichenachev, Y. Dudin, V. Velichansky, A. Zibrov, and S. Zibrov, "Eit-based vector magnetometry in linear polarized light," *arXiv preprint arXiv:1004.3969*, 2010.

[8] J. B. Khurgin, "Optical buffers based on slow light in electromagnetically induced transparent media and coupled resonator structures: comparative analysis," *JOSA B*, vol. 22, no. 5, pp. 1062–1074, 2005.

[9] D. J. Christle, A. L. Falk, P. Andrich, P. V. Klimov, J. U. Hassan, N. T. Son, E. Janzén, T. Ohshima, and D. D. Awschalom, "Isolated electron spins in silicon carbide with millisecond coherence times," *Nature materials*, vol. 14, no. 2, pp. 160–163, 2015.

[10] C. F. de las Casas, D. J. Christle, J. Ul Hassan, T. Ohshima, N. T. Son, and D. D. Awschalom, "Stark tuning and electrical charge state control of single divacancies in silicon carbide," *Applied Physics Letters*, vol. 111, no. 26, p. 262403, 2017.

[11] T. Bosma, J. Hendriks, M. Ghezellou, N. T. Son, J. Ul-Hassan, and C. H. van der Wal, "Broadband single-mode planar waveguides in monolithic 4h-sic," *Journal of Applied Physics*, vol. 131, no. 2, p. 025703, 2022.

[12] S. Hou, P.-E. Hellström, C.-M. Zetterling, and M. Östling, "550° c 4h-sic pin photodiode array with two-layer metallization," *IEEE Electron Device Letters*, vol. 37, no. 12, pp. 1594–1596, 2016.

[13] G. Chen, Y. Yu, and X. Zhang, "Optical phase erasure and wavelength conversion using silicon nonlinear waveguide with reverse biased pin junctions," *IEEE Photonics Journal*, vol. 7, no. 5, pp. 1–8, 2015.

[14] R. G. Hunsperger, *Integrated optics*, vol. 6. Springer, 2009.

[15] O. V. Zwier, T. Bosma, C. M. Gilardoni, X. Yang, A. R. Onur, T. Ohshima, N. T. Son, and C. H. van der Wal, "Electromagnetically induced transparency in inhomogeneously broadened divacancy defect ensembles in sic," *Journal of Applied Physics*, vol. 131, no. 9, p. 094401, 2022.

[16] M. Fleischhauer, A. Imamoglu, and J. P. Marangos, "Electromagnetically induced transparency: Optics in coherent media," *Reviews of modern physics*, vol. 77, no. 2, p. 633, 2005.

[17] Y. Huang, C. Min, and G. Veronis, "Subwavelength slow-light waveguides based on a plasmonic analogue of electromagnetically induced transparency," *Applied Physics Letters*, vol. 99, no. 14, p. 143117, 2011.

[18] B. E. Saleh and M. C. Teich, *Fundamentals of photonics*. john Wiley & sons, 2019.

[19] M. Fox, *Optical Properties of Solids*. Oxford Master Series in Physics, OUP Oxford, 2010.

[20] D. M. Sullivan, *Electromagnetic simulation using the FDTD method*. John Wiley & Sons, 2013.

[21] M. Hammer and O. V. Ivanova, "Effective index approximations of photonic crystal slabs: a 2-to-1-d assessment," *Optical and quantum electronics*, vol. 41, pp. 267–283, 2009.

[22] P. R. Berman, "Goos-Hänchen effect," *Scholarpedia*, vol. 7, p. 11584, Mar. 2012.

[23] M. Hammer, "Mode solver for 2-d multilayer waveguides, variational effective index approximation." https://www.siio.eu/eims.html. Accessed 13. Apr. 2023.

[24] M. Hammer, "Wave-matching mode solver for rectangular dielectric optical waveguides." https://www.siio.eu/wmms.html. Accessed 13. Apr. 2023.

[25] S. Sorieul, X. Kerbiriou, J. Costantini, L. Gosmain, G. Calas, and C. Trautmann, "Optical spectroscopy study of damage induced in 4h-sic by swift heavy ion irradiation," *Journal of Physics: Condensed Matter*, vol. 24, no. 12, p. 125801, 2012.

[26] F. Roccaforte, F. Giannazzo, F. Iucolano, J. Eriksson, M. Weng, and V. Raineri, "Surface and interface issues in wide band gap semiconductor electronics," *Applied Surface Science*, vol. 256, no. 19, pp. 5727–5735, 2010.

[27] D. Stefanakis and K. Zekentes, "Tcad models of the temperature and doping dependence of the bandgap and low field carrier mobility in 4h-sic," *Microelectronic Engineering*, vol. 116, pp. 65–71, 2014.

[28] S. Jalili and R. Majidi, "The effect of impurities on the electronic properties of mgo," *Physica B: Condensed Matter*, vol. 403, no. 19-20, pp. 3522–3526, 2008.

[29] C. Persson, U. Lindefelt, and B. Sernelius, "Band gap narrowing in n-type and p-type 3c-, 2h-, 4h-, 6h-sic, and si," *Journal of applied physics*, vol. 86, no. 8, pp. 4419–4427, 1999.

[30] M. Roschke and F. Schwierz, "Electron mobility models for 4h, 6h, and 3c sic [mesfets]," *IEEE Transactions on electron devices*, vol. 48, no. 7, pp. 1442–1447, 2001.

[31] J. Pernot, S. Contreras, J. Camassel, J. Robert, W. Zawadzki, E. Neyret, and L. Di Cioccio, "Free electron density and mobility in high-quality 4h–sic," *Applied Physics Letters*, vol. 77, no. 26, pp. 4359–4361, 2000.

[32] E. Marcatili, "Bends in optical dielectric guides," *Bell System Technical Journal*, vol. 48, no. 7, pp. 2103–2132, 1969.

[33] R. G. Hunsperger, A. Yariv, and A. Lee, "Parallel end-butt coupling for optical integrated circuits," *Applied optics*, vol. 16, no. 4, pp. 1026–1032, 1977.

[34] Thorlabs, "Pm1300-xp polarization-maintaining single mode optical fiber." https://www.thorlabs.com/newgrouppage9.cfm?objectgroup_id=1596. Accessed 14. Jun. 2023.

[35] P. Karioja and D. Howe, "Diode-laser-to-waveguide butt coupling," *Applied optics*, vol. 35, no. 3, pp. 404–416, 1996.

[36] S. Wang, M. Zhan, G. Wang, H. Xuan, W. Zhang, C. Liu, C. Xu, Y. Liu, Z. Wei, and X. Chen, "4h-sic: a new nonlinear material for midinfrared lasers," *Laser & Photonics Reviews*, vol. 7, no. 5, pp. 831–838, 2013.

[37] E. Optics, "Gaussian beam propagation." https://www.edmundoptics.com/knowledge-center/application-notes/lasers/gaussian-beam-propagation. Accessed 21. Jun. 2023.

[38] M. Hammer, "1-d mode solver for slab waveguide bends." https://www.siio.eu/bends.html. Accessed 13. Apr. 2023.

[39] A. Optics, "Mode - eigenmode expansion (eme) solver introduction." https://optics.ansys.com/hc/en-us/articles/360034396614-MODE-EigenMode-Expansion-EME-solver-introduction. Accessed 3. Jul. 2023].

[40] Y. Jiao, J. Liu, A. M. Mejia, L. Shen, and J. van der Tol, "Ultra-sharp and highly tolerant waveguide bends for inp photonic membrane circuits," *IEEE Photonics Technology Letters*, vol. 28, no. 15, pp. 1637–1640, 2016.

[41] M. Hammer, "1-d mode solver for complex optical multilayer step-index slab waveguides." https://www.siio.eu/plass.html. Accessed 13. Apr. 2023.

[42] A. Yi, C. Wang, L. Zhou, Y. Zhu, S. Zhang, T. You, J. Zhang, and X. Ou, "Silicon carbide for integrated photonics," *Applied Physics Reviews*, vol. 9, no. 3, 2022.

[43] A. Chanana, H. Larocque, R. Moreira, J. Carolan, B. Guha, E. G. Melo, V. Anant, J. Song, D. Englund, D. J. Blumenthal, *et al.*, "Ultra-low loss quantum photonic circuits integrated with single quantum emitters," *Nature Communications*, vol. 13, no. 1, p. 7693, 2022.

[44] A. E. Siegman, *Lasers*. University science books, 1986.

Appendix

In the following sections we present some additional information about the methods and results used in this thesis. First of all, we are going to look at the electric-field distribution, as predicted by our solver, which is used to solve equation (10). Secondly, an image from the diffraction pattern, used to roughly align the optical fiber to the sample, as captured from camera 2 will be shown. Thirdly, we will look at some addition results, which are subdivided into three sections. At first, we compare the free-carrier losses in a slab waveguide according to three solvers. We show that 21 is a valid equation for calculating theses losses. Afterwards, we will look at how changing the doping concentration for the cladding and substrate layer impacts these losses. Finally, a raw data image, which is used for the angular alignment protocol and Figure 20 is shown and explained.

A Electric-field distribution of our solver

In Figure 22 the vertical and horizontal component of the electric-field, as predicted by our solver, is shown. By multiplying these two solution and squaring the result one find the intensity distribution shown in Figure 7(a) in section **2.2.4**. It is important to note that y and z do not denote any form of polarisation, as they are both TE_0 modes. Instead y and z denote the electric/intensity distribution over a geometric space.

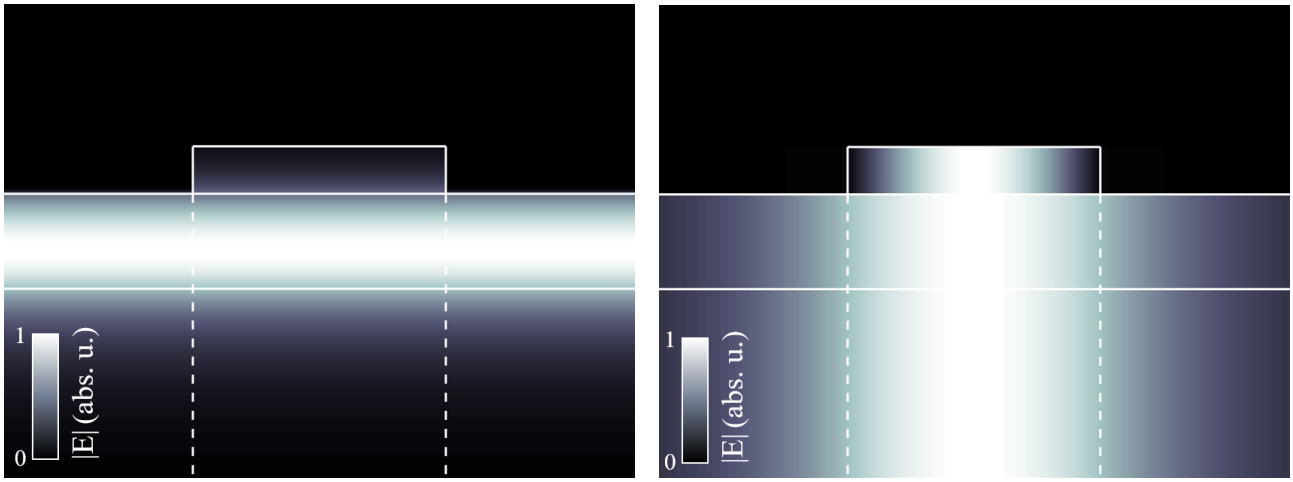

(a) Electric-field distribution along z-axis (b) Electric-field distribution along y-axis

Figure 22: One dimensional independent vertical and horizontal TE_0 solutions to the strip-loaded waveguide electric-field distributions. By multiplying theses solutions, as given by equation (10), one finds the two dimensional electric-field distribution. By squaring this two dimensional distribution one find the intensity of the TE_00 mode as depicted in Figure 7(a). (a) Electric-field distribution along z-axis, also known as F(z) in equation (10). (b) Electric-field distribution along y-axis, also known as G(y) in equation (10).

B Experimental Setup

In Figure 23 a diffraction pattern at the waveguide end-facet is visible from camera 2. The (two) white lobes above the waveguide surface (black to gray transition) is used for rough alignment of the optical fiber. Namely, when these patterns disappears we know that we have crossed the surface of the waveguide.

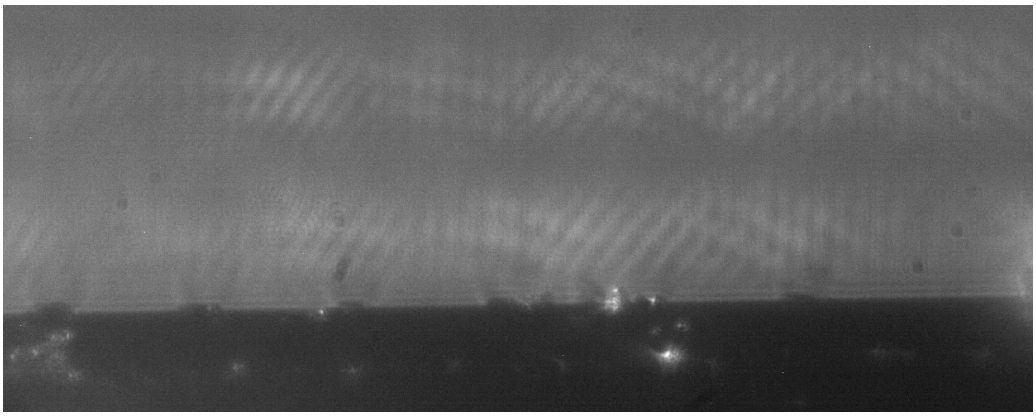

Figure 23: Diffraction pattern visible (white lobes) above the waveguide (black to gray transition), which is used to roughly align the optical fiber to get an initial signal. The total width of the image is around 300 μm.

C Results

In the following section a few additional results are presented. First we will compare the free-carrier losses for a slab waveguide as predicted by three different methods/solvers. Secondly, we will look at how changing the doping concentration in the cladding and substrate can change the free-carrier losses. Finally, we will show a plot of the raw data we used during for the angular alignment method, which will explain how we got the plots in Figure 20.

C.1 Comparing different solvers free-carrier losses

In Table 4 the free-carrier losses calculated in a slab waveguide, by our solver and WMMS using equation (21) and PlasS, is shown. This was done to check the validity of the equation, because PlasS only works in one dimension. Therefore, there was no direct way to compare the results for a strip-loaded waveguide. Since the losses between all methods are almost identical, it was concluded that equation (21) can be used to calculate the free-carrier losses.

Table 4: Free carrier absorption losses in a p-i-n slab waveguide, according to three different methods of calculation.

Method	$\mathcal{L}$oss (dB/cm) p-i-n	$\mathcal{L}$oss (dB/cm) n-i-n
Our solver + eq. (21)	11.3	10.3
WMMS + eq. (21)	11.0	10.4
PlasS	11.0	10.3

C.2 Effect of doping concentration on losses

It was shown that our waveguide has losses on the order of 10 dB/cm, which limits the waveguide to on chip applications. If for some reason the required length of this type of waveguide has to be longer than 1 cm, then free-carrier absorption has to be reduced. According to equation (11) the attenuation constant depends linearly on the doping concentration N. However, for doping concentrations between 10^{16} and 10^{19} cm^{-3} there is also a ten times reduction in the free-carrier mobility (μ) [27][30][31]. The doping concentration has therefore a significant impact on the amount of free-carrier absorption. In addition, it is relatively simple to influence during manufacturing. To calculate the free-carrier losses for different doping concentrations also includes calculating all the different EM-field distributions, because the doping concentration also affects the real refractive index. We do not consider the divergence or changes in the beam profile as it propagates through the waveguide. In reality this does happen, but we have shown in section **4.3** that we can simply take the static beam profile according to Figure 7(a) and apply equation (21) to get an accurate description of the losses. The results are identical to PlasS, which does solve for the beam divergence as it travels through the waveguide. This simplifies the problem greatly, as we do not have to solve for the beam propagation. However, still due to the large amount of computational power required, it was decided to only solve for a slab waveguide and not for a strip-loaded waveguide. But, with a few more weeks of work this method can also be extended to the strip-loaded waveguide.

In Figure 24 the losses of said slab waveguide for n- and p-type doping concentrations ranging from (1 to 250)$\cdot 10^{17}$ cm^{-3} in the cladding layer and (1 to 100)$\cdot 10^{17}$ cm^{-3} in the substrate layer are shown. The doping concentration for our samples are marked with a black cross. The white regions near the axes show the combination of doping concentration where no modes exists. The white cone area in the top-middle are combinations of doping concentration, where higher order modes exist. We are only interested in zero-order modes and this region is therefore excluded. We have also drawn contours of constant loss values at intervals of 2 dB/cm. We see that if the doping concentrations in both the cladding and substrate are halved, then the amount of losses also reduce by a factor of a half. However, it is difficult to reach values lower than 4 dB/cm by reducing the doping concentration. Because, as we lower the doping concentrations, the contrast in the real refractive index reduces. This results in less confinement in the core layer and more light will be in the substrate/cladding layer, which in turn will increase the losses due to the higher attenuation in these layers. For our applications we want to maximise the confinement and therefore it is not in our interest to lower the doping concentration to reduce losses.

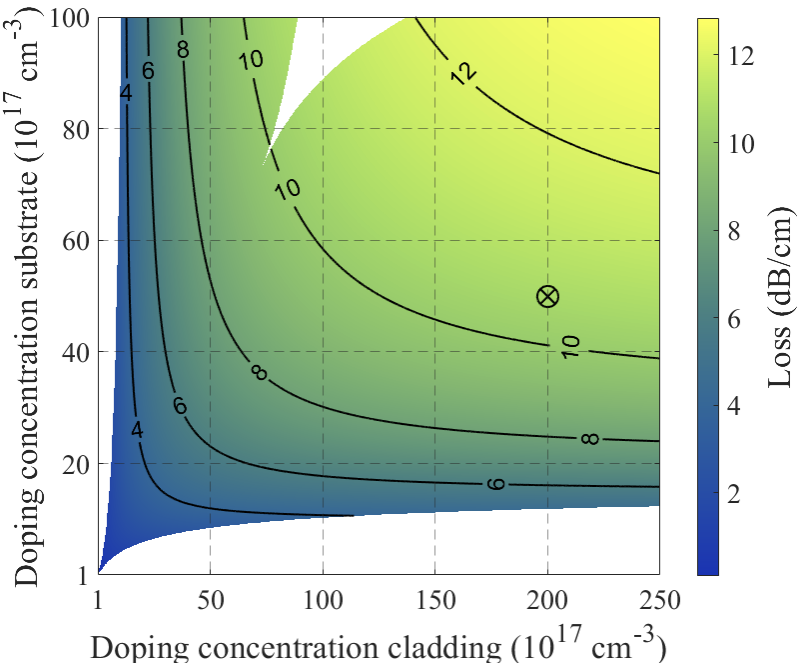

(a) n-type doped cladding layer

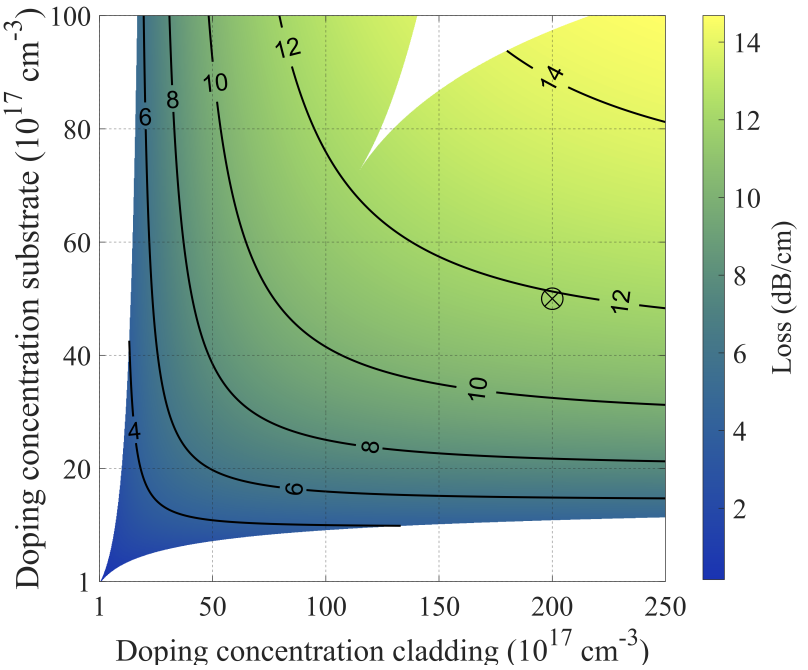

(b) p-type doped cladding layer.

Figure 24: Losses (dB/cm) due to free-carrier absorption for different doping types and concentrations in the substrate and cladding layers, where the black cross marks the doping levels in our samples. The white areas near the axis have no waveguiding solutions, whereas the white area located in the top center allows for higher order modes.

C.3 Angular Alignment Method

In Figure 25 a 3D-plot of the raw data used for the angular alignment protocol is shown. Here we have scanned over a range of y and x values, by first moving along the y-axis and measuring the photodiode (PD) signal. This results in a Gaussian shape of the PD voltage as a function of y-axis location. The maximum value of this Gaussian is determined and saved. Afterwards, the optical fiber is retracted along the x-axis by 1 µm and the previous steps are repeated. The red trace in Figure 25 shows the location of maximum transmission for all x values. This trace is then plotted versus the x-axis and what results are the plots in Figure 20. The slope of this red trace is approximately the offset angle and this is therefore how we are able to align the optical fiber.

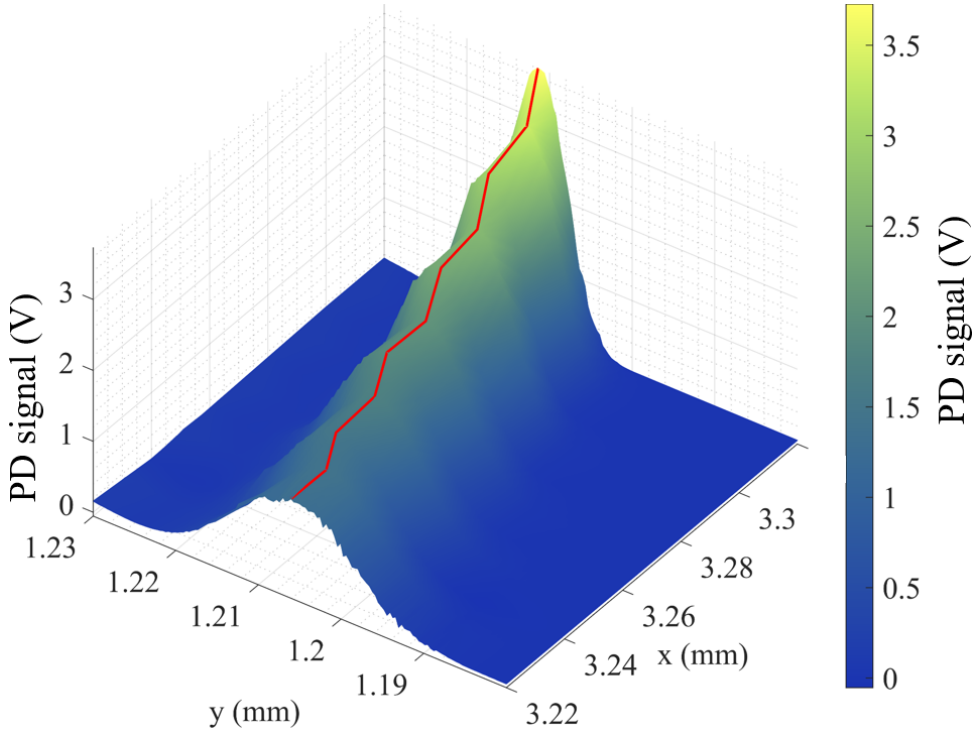

Figure 25: Raw photodiode (PD) signal in volts of a x, y scan, used for the angular alignment method. Red line traces the maximum transmission for every x-axis value. This red trace is plotted in 2D, as shown in Figure 20. The slope of this trace is approximately the offset angle α.